Cancer Cell

Article

Immune determinants of CAR-T cell expansion in solid tumor patients receiving GD2 CAR-T cell therapy

Graphical abstract

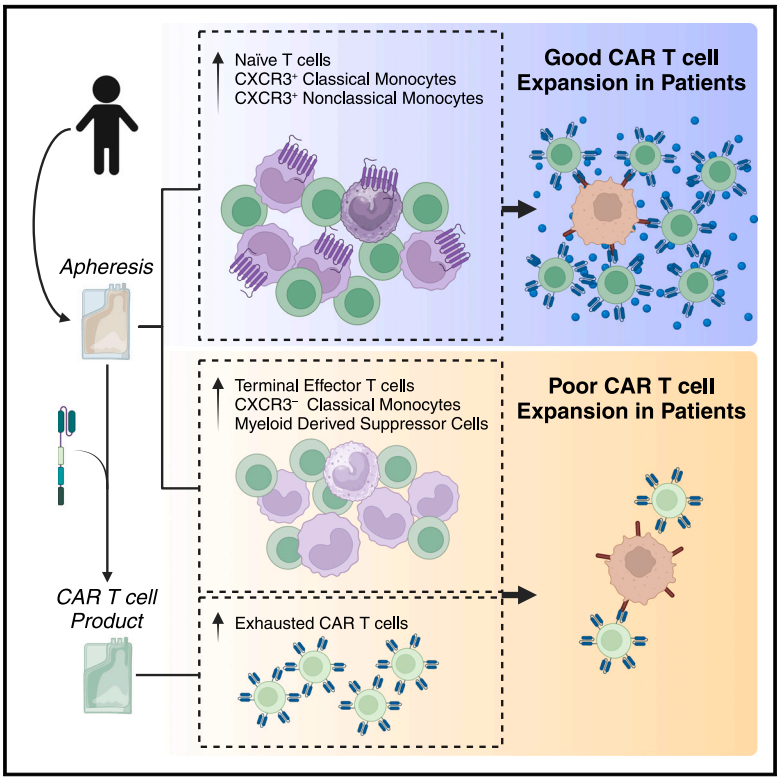

Highlights

- GD2 CAR-T Phase I trial shows feasibility and safety in osteosarcoma and neuroblastoma
- Multi-omic analyses identify immune contributors to CAR-T expansion in patients
- Good expanders had increased naive T cells and CXCR3^{+} monocytes at baseline
- Poor expanders had more CXCR3^{-} monocytes at baseline and exhausted CAR-T product

Authors

Sabina Kaczanowska, Tara Murty, Ahmad Alimadadi, ..., Crystal L. Mackall, Sneha Ramakrishna, Rosandra N. Kaplan

Correspondence

ramakrs@stanford.edu (S.R.), rosie.kaplan@nih.gov (R.N.K.)

In brief

Chimeric antigen receptor T cell (CAR-T) therapy targeting GD2 in osteosarcoma and neuroblastoma in a Phase I clinical trial shows feasibility and safety but limited efficacy. Kaczanowska et al. analyze baseline, product and post-treatment patient samples and demonstrate myeloid and T cell phenotypes associated with CAR-T expansion.

Kaczanowska et al., 2024, Cancer Cell *42*, 35–51
January 8, 2024 Published by Elsevier Inc.
https://doi.org/10.1016/j.ccell.2023.11.011

CellPress

Cancer Cell

CellPress

Article

Immune determinants of CAR-T cell expansion in solid tumor patients receiving GD2 CAR-T cell therapy

Sabina Kaczanowska,[1,14] Tara Murty,[2,14] Ahmad Alimadadi,[3,4,5,14] Cristina F. Contreras,[1,13] Caroline Duault,[6] Priyanka B. Subrahmanyam,[6] Warren Reynolds,[2] Norma A. Gutierrez,[3] Reema Baskar,[7] Catherine J. Wu,[8,9] Franziska Michor,[8] Jennifer Altreuter,[8] Yang Liu,[8] Aashna Jhaveri,[8] Vandon Duong,[2] Hima Anbunathan,[2] Claire Ong,[1] Hua Zhang,[1] Radim Moravec,[10] Joyce Yu,[9] Roshni Biswas,[9] Stephen Van Nostrand,[9] James Lindsay,[9] Mina Pichavant,[4] Elena Sotillo,[2] Donna Bernstein,[1] Amanda Carbonell,[1] Joanne Derdak,[1] Jacquelyn Klicka-Skeels,[1] Julia E. Segal,[1] Eva Dombi,[1] Stephanie A. Harmon,[11] Baris Turkbey,[11] Bita Sahaf,[2] Sean Bendall,[5] Holden Maecker,[4] Steven L. Highfill,[12] David Stroncek,[12] John Glod,[1] Melinda Merchant,[1] Catherine C. Hedrick,[3,4,5] Crystal L. Mackall,[2] Sneha Ramakrishna,[2,15,*] and Rosandra N. Kaplan[1,15,16,*]

[1]Pediatric Oncology Branch, Center for Cancer Research, National Cancer Institute, National Institutes of Health, Bethesda, MD, USA
[2]Center for Cancer Cell Therapy, Stanford Cancer Institute, Stanford University School of Medicine, Stanford, CA, USA
[3]La Jolla Institute for Immunology, La Jolla, CA, USA
[4]Immunology Center of Georgia, Augusta University, Augusta, GA, USA
[5]Georgia Cancer Center, Medical College of Georgia at Augusta University, Augusta, GA, USA
[6]Stanford Human Immune Monitoring Center, Stanford University School of Medicine, Stanford, CA, USA
[7]Department of Pathology, Stanford University, Stanford, CA, USA
[8]Broad Institute, Cambridge, MA, USA
[9]Dana-Farber Cancer Institute, Boston, MA, USA
[10]Cancer Therapy Evaluation Program, National Cancer Institute, National Institutes of Health, Bethesda, MD, USA
[11]Artificial Intelligence Resource, Molecular Imaging Branch, National Cancer Institute, National Institutes of Health, Bethesda, MD, USA
[12]Center for Cellular Engineering, Department of Transfusion Medicine, National Institutes of Health Clinical Center, Bethesda, MD, USA
[13]Department of Oncology, University of Oxford, Oxford, UK
[14]These authors contributed equally
[15]Senior author
[16]Lead contact
*Correspondence: ramakrs@stanford.edu (S.R.), rosie.kaplan@nih.gov (R.N.K.)
https://doi.org/10.1016/j.ccell.2023.11.011

SUMMARY

Chimeric antigen receptor T cells (CAR-Ts) have remarkable efficacy in liquid tumors, but limited responses in solid tumors. We conducted a Phase I trial (NCT02107963) of GD2 CAR-Ts (GD2-CAR.OX40.28.z.iC9), demonstrating feasibility and safety of administration in children and young adults with osteosarcoma and neuroblastoma. Since CAR-T efficacy requires adequate CAR-T expansion, patients were grouped into good or poor expanders across dose levels. Patient samples were evaluated by multi-dimensional proteomic, transcriptomic, and epigenetic analyses. T cell assessments identified naive T cells in pre-treatment apheresis associated with good expansion, and exhausted T cells in CAR-T products with poor expansion. Myeloid cell assessment identified CXCR3^{+} monocytes in pre-treatment apheresis associated with good expansion. Longitudinal analysis of post-treatment samples identified increased CXCR3^{-} classical monocytes in all groups as CAR-T numbers waned. Together, our data uncover mediators of CAR-T biology and correlates of expansion that could be utilized to advance immunotherapies for solid tumor patients.

INTRODUCTION

Children and young adults with recurrent, metastatic, or unresectable osteosarcoma or neuroblastoma experience dismal outcomes, with little progress in osteosarcoma treatment options over the last several decades.[1–7] In these patients, immunotherapy provides an enticing opportunity to change the treatment paradigm by targeting tumor-specific antigens. In fact, neuroblastoma has seen improvement in overall survival for high-risk patients using a disialoganglioside glycoprotein 2 (GD2)-targeting monoclonal antibody, which is now part of frontline therapy.[8] Based on this, several trials have tested GD2-targeting chimeric antigen receptor T cells (CAR-Ts) in neuroblastoma and have shown safety, but limited efficacy.[9–12] Understanding the basis of this limited efficacy is crucial for the progress of solid tumor CAR-T therapies. Experience with

Table 1. Patient Demographics and Baseline Characteristics

Characteristic		Number of patients enrolled in clinical trial (n=15)	Number of patients who received GD2 CAR-Ts (n=13)
Age	Median (range)	17 (8 - 28) years	18 (10 - 28) years
Sex	Female/Male	3/12	3/10
Race	White	9	7
	African American	3	3
	Asian	1	1
	Hispanic	1	1
	Multiple Race	1	1
Tumor Type	Osteosarcoma	12	11
	Neuroblastoma	3	2
Prior Therapies	Surgery	14	12
	Chemotherapy	15	13
	Radiation	8	6
	Immunotherapy / Targeted Therapy	6	5
	Autologous Stem Cell Transplant	3	2
	Total Lines of Prior Systemic Therapy		
	1– 2	5	5
	3 – 4	7	6
	5 or more	3	2
Performance Status	ECOG 0	3	3
	ECOG 1	10	9
	ECOG 2	2	1

CAR-T therapies in both solid and hematologic malignancies has identified CAR-T expansion as an essential first step toward CAR-T efficacy.[13] As such, progress in solid tumor CAR-Ts requires understanding mediators of CAR-T expansion. Therefore, we report a GD2.CD28.OX40.z CAR-T trial in neuroblastoma and osteosarcoma, where we performed robust correlative studies to shed light on mediators of CAR-T expansion in patients.

Biomarker evaluations of CAR-Ts in acute lymphoblastic leukemia and chronic lymphocytic leukemia correlate early memory T cell phenotypes in patient pre-treatment apheresis with CAR-T success.[14,15] Conversely, less abundant early memory T cell populations correlate with decreased T cell expansion potential.[16] Additionally, exhausted T cells are associated with poor clinical response.[17,18] In the clinical solid tumor space, comprehensive immune cell analyses are scarce. Thus far, central memory cells in patient GD2.CD3z CAR-T products are associated with more durable remissions,[10] and pre-clinical models of GD2 CAR-Ts identify tonic signaling and exhaustion as a limitation of CAR-T activity.[19,20] As CAR-T therapies continue to gain traction in the treatment of solid tumors, it will be important to validate and expand on these potential biomarkers of CAR-T activity specifically in the context of solid tumors.

In addition to identifying features of T cells, there is a shift in focus as the contributions of myeloid cells to cancer progression and immunotherapy efficacy become increasingly apparent.[21] In patients treated with GD2.CD28.OX40.z CAR-Ts, myeloid populations expand after CAR-T administration.[11] Moreover, in patients with diffuse midline glioma treated with GD2.41BB.z CAR-T therapy, suppressive myeloid cells may have limited CAR-T activity.[22] These insights into myeloid populations underscore the importance of deeper investigation into their roles to unlock the full potential of immunotherapy for solid tumor patients.

Here, we demonstrate the safety and feasibility of administering a third-generation GD2.CD28.OX40.z CAR-T to GD2^{+} osteosarcoma and neuroblastoma patients. Naive and memory T cell as well as CXCR3^{+} myeloid populations in pre-treatment apheresis show striking correlation with CAR-T expansion and may be predictive of patient response to immunotherapies. These findings highlight the power of integrating clinical outcomes with robust correlative analyses to provide insight into the T cell and myeloid immune milieu modulating CAR-T activity in solid tumor patients.

RESULTS

Patient characteristics and CAR-T manufacturing feasibility

Fifteen patients, twelve with osteosarcoma and three with neuroblastoma, were enrolled in this Phase I single center clinical trial (NCT02107963) testing GD2.CD28.OX40.z CAR-Ts (Table 1, Figures 1A, 1B, and Table S1). The median age was 17 (range 8–28), and these patients were all heavily pre-treated prior to enrollment with multiple modalities of therapies (Table 1). Disease burden at baseline varied on the metrics of tumor size, number of metastatic lesions, and number of sites involved (Tables 2 and 3). Thirteen patients received the intended GD2 CAR-Ts at the four planned dose levels (1 x 10^5, 1 x 10^6, 3 x 10^6, and 1 x 10^7 transduced GD2 CAR-Ts/kg), and two patients died prior to CAR-T administration. GD2 CAR-Ts were manufactured using a retroviral vector (iC9-2A-14G2A.CD28.OX40Z), activated by

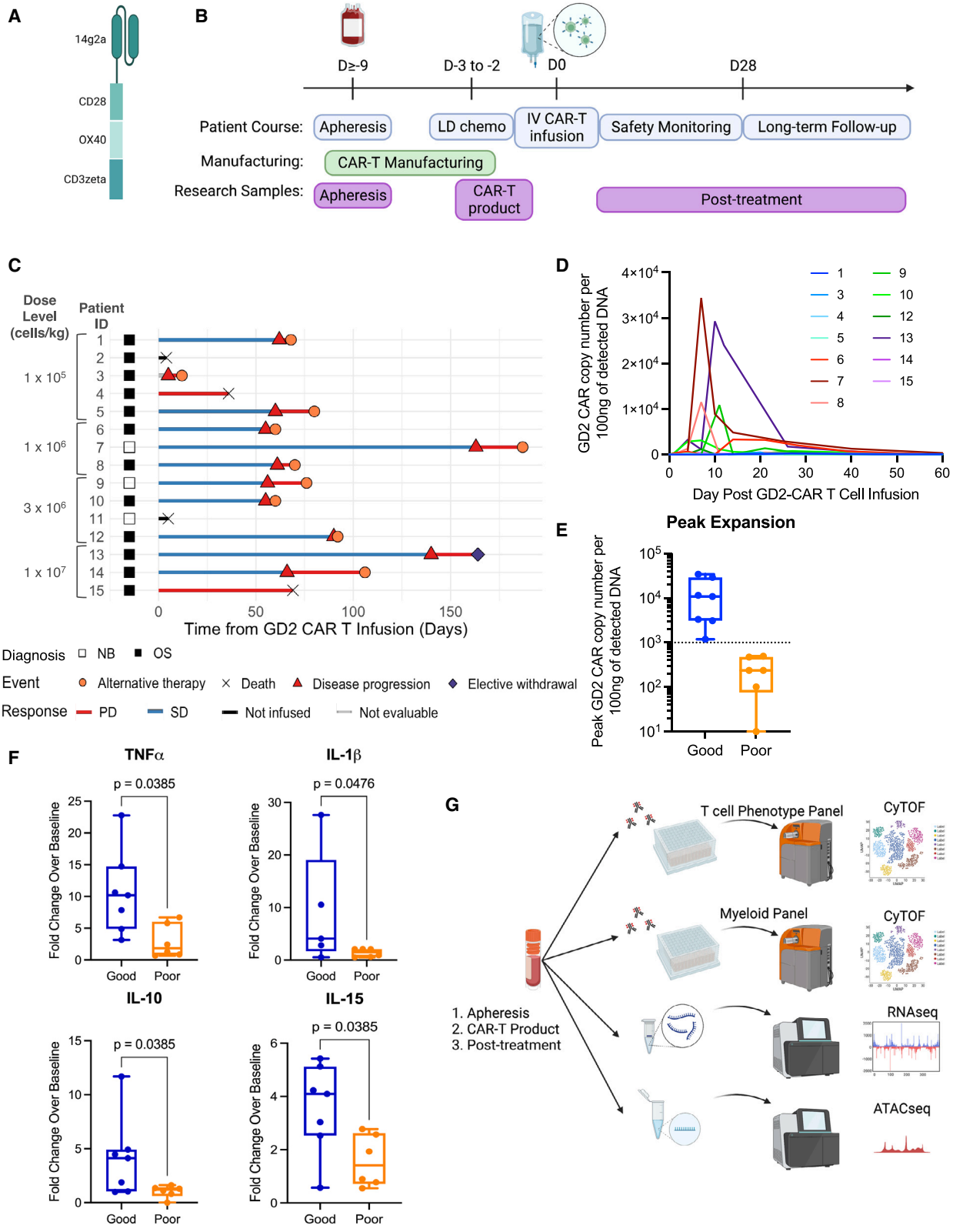

Figure 1. GD2 CAR-T administration results in varying levels of CAR-T expansion

(A) Schematic of GD2 CAR-T construct.

(B) Timeline of treatment and sample collection for patients receiving GD2 CAR-T.

(legend continued on next page)

CD3/CD28 beads and expanded in the presence of IL-2 (Figure S1A). The cell selection process prior to manufacturing changed from bead selection to elutriation + ACK lysis for the last four treated patients to reduce myeloid populations during the manufacturing culture process,[23] which resulted in improved GD2 CAR-T expansion during manufacturing (Figures S1A and S1B). One patient's cells failed transduction/expansion based on the final number of GD2 CAR-T-transduced cells (6 x 10^6 cells at harvest), but the product was able to be re-manufactured with the addition of Ficoll density gradient and monocyte-adhesion steps. All GD2 CAR-T products were manufactured within 10–11 days and met release criteria as specified on the clinical trial protocol (Table S2).

Toxicity and response

Safety was assessed during the study through the evaluation of treatment emergent adverse events (TEAEs), laboratory profiles, physical examinations, and vital signs. TEAEs were graded according to the National Cancer Institute Common Terminology Criteria for Adverse Events, version 4.0. Overall, GD2 CAR-Ts were very well tolerated without significant evidence of toxicity attributed to CAR-T (Table S3). 15.4% (2/13) of patients experienced grade-1 cytokine release syndrome without signs of neurological toxicities. No dose-limiting toxicities attributed to the IND research were observed in any of the dose levels of administration. No patients required administration of the iCasp9 suicide gene switch, AP1903 (rimiducid), for unacceptable toxicity possibly, probably, or likely related to GD2 CAR-Ts. On day 28 following GD2 CAR-T infusion, 16.7% (2/12) of evaluable patients had progressive disease and 83.3% (10/12) had stable disease (SD). 30% (3/10) of SD patients remained stable at 60 days post-GD2 CAR-T infusion, but all patients eventually progressed (Figure 1C).

CAR-T kinetics and activity

While subsequent CAR-T trials have since implemented fludarabine and cyclophosphamide for lymphodepletion, this trial used only cyclophosphamide at 1800 mg/m^2/day for two days, resulting in a nadir in absolute lymphocyte count occurring between day 0 and 7 in all patients (Figure S1C) and was shorter than patients receiving a fludarabine/cyclophosphamide regimen.[24] We measured the expansion and persistence of GD2 CAR-Ts in the peripheral blood using qPCR. GD2 CAR-Ts expanded in all patients receiving treatment, half of whom had expansion above 1,000 GD2 CAR copies/100 ng DNA, a level similar to that seen in clinically active CD19 and CD22 CAR-Ts,[25–27] but the GD2 CAR-Ts had limited persistence (Figures 1D and 1E). CAR-T expansion in patients did not associate with dose level, CAR transduction efficiency, nor CD4/8 ratio in the CAR-T product (Figures S1D, S1E, and Table S2). Importantly, this trial, similar to all Phase I clinical trials, enrolled patients who were relapsed and frequently metastatic, but demonstrated considerable differences in disease burden. We developed a disease burden score, based on metrics of tumor size, number of metastatic lesions, and number of sites involved at time of trial enrollment (Table 2). This score correlated closely with an AI-generated disease burden quantification[28] and together may be useful to quantify tumor burden and potentially correlate with treatment response in the clinical trial setting. Surprisingly, these patient disease burden metrics did not correlate with GD2 CAR-T expansion in patients (Figure S1F and Table 3). Importantly, peak GD2 CAR-T expansion (maximum level detected at available time points) above 1,000 GD2 CAR copies/100 ng DNA did associate with increased cytokine levels in patient plasma on day 10 ± 4 days (range day 7–14), suggesting a functional difference in these patients' CAR-Ts and confirming the importance of common cytokine receptor γ-chain family of cytokines, such as IL-15, as drivers of T cell expansion, consistent with other adoptive cell therapy studies[24] (Figures 1F and S2). Additionally, all patients with CAR-T expansion over 1,000 copies/100 ng DNA demonstrated stable disease, whereas 3 of 5 patients with CAR-T expansion below 1,000 copies/100 ng DNA had progressive disease within the 28-day window (Figure 1C).

Table 2. Disease Burden Score

Size of largest tumor lesion	Number of metastatic lesions ≥ 1 cm in size	Number of sites involved*
≤ 2.5 cm; 0 points	≤ 3; 0 point	1; 0 point
> 2.5 cm, ≤ 5 cm; 1 point	>3, ≤ 6; 1 point	2-3; 1 point
> 5 cm; 3 points	> 6; 3 points	4 or more; 3 points

Scoring:
Total score ≤ 2, small disease burden
Total score ≥ 3, large disease burden
*Sites: CNS (brain and spine), head/neck (not CNS), chest, abdomen, pelvis, upper extremity, lower extremity

Based on these findings, we categorized patients into those with good CAR-T expansion (peak CAR-T expansion >1,000 GD2 CAR copies/100 ng DNA) versus poor CAR-T expansion (peak CAR-T expansion <1,000 GD2 CAR copies/100 ng DNA) (Figure 1E). To profile the cellular correlates of CAR-T expansion and activity in these patients, we performed comprehensive phenotypic (cytometry by time-of-flight [CyTOF]), transcriptomic (RNA sequencing [RNA-seq]), and epigenetic (assay for transposase-accessible chromatin with high-throughput sequencing [ATAC-seq]) analyses of patient pre-treatment apheresis (*apheresis*), CAR-T product (*product*), and peripheral blood mononuclear cells collected between day 1 and 60 after CAR-T infusion (*post-treatment*) (Figure 1G).

(C) Swimmer's plot representing patient response from time of GD2 CAR-T infusion.
(D) Levels of CAR-T detected in the peripheral blood of patients as measured by qPCR of the GD2 CAR-T construct.
(E) Stratification of patients into good and poor CAR-T expanders based on peak (maximum) level of GD2 CAR-T detected by qPCR. Boxplot represents all patients (dots) with median (line) and range (whiskers).
(F) Fold change of cytokines in the plasma of patients on day 10 ± 4 (range day 7–14) following CAR-T administration over day 0 prior to CAR-T administration. Boxplot represents all patients (dots) with median (line) and range (whiskers). Statistical analysis conducted by Mann-Whitney test (n = 13).
(G) Schematic of patient samples pre-treatment apheresis, CAR-T product, and post-treatment (day 1–60 after CAR-T infusion) multi-dimensional analyses, including proteomic (mass cytometry or CyTOF), transcriptomic (RNA-seq), and epigenetic (ATAC-seq) assays. Also see Figures S1, S2, and Tables S1–S3.

Table 3. Disease burden at baseline does not correlate with CAR-T Peak Expansion

Patient	SUV max	Total Lesion Glycolysis (SUVbw*ml)	Volume (ml)	Disease burden score	GD2 CAR-T Peak Expansion
1	4.49	11.71	5.34	1, small	237.2
2	27.96	7997.11	1304.95	7; large	N/A (no CAR)
3	11.83	4559.04	1054.72	7; large	494.9
4	102.88	2102.47	355.8	7; large	0.0
5	16.08	129.47	28.52	2; small	237.3
6	14.18	348.3	90.93	5; large	3331.7
7	*incomplete imaging for evaluation			*small	34400.0
8	10.89	167.46	42.31	1; small	11500.0
9	3.72	4.44	2.23	0; small	10875.0
10	11.03	1405.28	413.2	5; large	3100.0
11	*incomplete imaging for evaluation			*large	N/A (no CAR)
12	9.03	576.05	182.21	4; large	1185.6
13	11.26	101.18	20.16	1; small	29269.0
14	5.4	253.56	83.21	1; small	100.6
15	15.59	330.98	85.41	3; large	471.5

Good and poor expanders exhibit shared immune cell populations in CAR-T products and post-treatment samples

CyTOF analysis of GD2 CAR-T products using a robust T cell Phenotype Panel identified 8 distinct clusters, none of which were differentially represented between good and poor expanders (Figures 2A—2C, S3A, and S3B). Interestingly, two clusters comprised an average of 63% of each patient's CAR-T product (Figure 2D). These GD2 CAR$^+$ T cell clusters define a proliferating, activated population of CD4 T cells (cluster 3; CD39$^+$KI67$^+$ CD45RO$^+$ CD95$^+$OX40$^+$CTLA4$^+$CD38$^+$TBET$^+$BTLA$^+$) and CD8 T cells (cluster 6; CD39$^+$KI67$^+$CD45RO$^+$CD95$^+$CTLA4$^+$CD38$^+$ TBET$^+$BTLA$^+$) (Figure 2D). Application of a CAR-T Exhaustion Score based on bulk RNA-seq data (Figure S3C), developed from a previously published dataset,[29] suggested trends of increased activation signatures in good expanders and increased exhaustion signatures in poor expanders (Figure 2E). Finally, epigenetic analyses of CAR-T products via ATAC-seq also demonstrated limited differences in the open chromatin (Figures 2F and S4), but showed enrichment in good expander CAR-T products of AP-1 factor transcription factor (TF) motifs, such as BATF, JUN, and FOS, signals previously implicated in exhaustion-resistant T cells[29] (Figure 2G). When evaluating post-treatment samples by CyTOF, poor expanders demonstrated a trend of increased CD39 and Helios protein expression, consistent with exhaustion[30,31] and T regulatory cells (Tregs)[32] (Figure S3D). Together, these data demonstrate that while all CAR-T products have similar proteomic exhaustion signatures, poor expanders have increased transcriptomic signatures of exhaustion and good expanders have increased epigenetic signatures of exhaustion resistance, potentially contributing to CAR-T expansion and persistence in patients.

Good CAR-T expansion associates with increased T cell memory subsets in apheresis prior to CAR-T manufacturing

Prior to CAR-T manufacturing, patient cells are collected via apheresis for CAR-T production. We posited that these apheresis samples represent the detailed circulating immune milieu of patients at baseline. Phenotypic profiling of the apheresis samples by CyTOF using the T cell Phenotype Panel identified twelve distinct clusters from all viable CD45$^+$ cells, ten of them within the T cell compartment (Figures 3A—3C and S3E). Comparison of samples originating from good versus poor expanders identified two significantly differentially abundant clusters: cluster 1, a naive CD8 T cell population (CD45RA$^+$CCR7$^+$) associated with good CAR-T cell expansion, and cluster 4, a terminal effector TEMRA CD8 T cell population (CD45RA$^+$CCR7$^-$CD38$^+$ TBET$^+$CD11b$^+$CD122$^+$) trended with poor CAR-T expansion (Figure 3D). Manual gating of apheresis memory populations based on expression of CD45RA and CCR7 confirmed that naive (CD45RA$^+$CCR7$^+$) CD4 and CD8 T cells trend toward increased proportions in good expanders, while effector TEMRA (CD45RA$^+$CCR7$^-$) and effector (CD45RA$^-$CCR7$^-$) CD4 and CD8 T cell populations were predominant in poor expanders (Figure 3E). Random forest analysis of surface markers measured by CyTOF identified CD38, previously implicated in antigen-induced T effector function,[33] as a prominent marker in apheresis associated with poor expansion (Figure S3F). Although transcriptomic analysis by RNA-seq resulted in a small number of differentially expressed genes between good and poor expanders (Figure S3G), Gene Set Enrichment Analysis (GSEA) focusing on transcriptomic profiles that define T cell subtypes identified enrichment of gene sets associated with naive or central memory phenotypes in apheresis from good expanders compared to poor expanders (Figure 3F). Conversely, GSEA analysis demonstrated enrichment of Treg and IL-4 gene sets in poor CAR-T expanders, a finding aligned with recent publications identifying Tregs as a potential inhibitor of CAR-T response[34,35] (Figure 3F). These findings illustrate that naive T cell populations in apheresis correlate with good CAR-T expansion, whereas TEMRA T cell populations in apheresis associate with poor expansion.

Finally, we profiled the epigenetic landscape of apheresis samples by ATAC-seq. Principal component analysis separated samples according to their expansion and showed increased

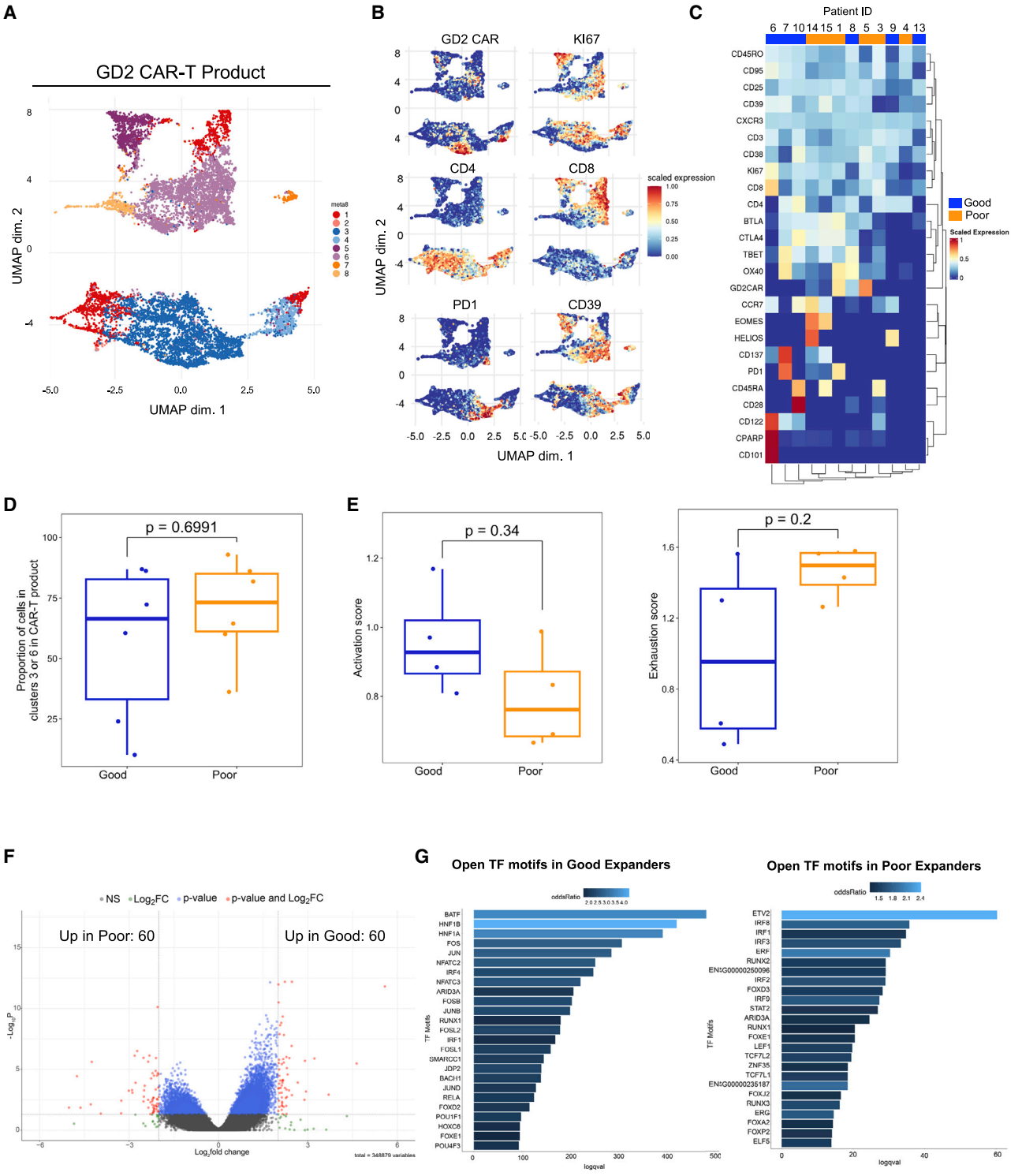

Figure 2. CAR-T product samples display features of T cell exhaustion

(A) UMAP plot of T cell populations in GD2 CAR-T product using the T cell Phenotype CyTOF Panel (n = 12 patients).

(B) Feature plots showing the distribution of expression of select CyTOF markers among the T cell populations.

(C) Heatmap of hierarchical clustering of median marker expression in GD2 CAR-T product by CyTOF represented per patient.

(D) Proportion of total cells represented in T cell Phenotype Panel clusters 3 and 6. Boxplot represents all patients (dots) with median (line) and range (whiskers). Statistics calculated by Mann-Whitney test (n = 12 patients).

(legend continued on next page)

genome-wide accessibility of chromatin in good versus poor expanders (Figures 3G, 3H, and Figure S4). TFs associated with T cell dysfunction and regulatory roles, including Epas1, TCF4, and Gli2, were enriched in poor expanders[36] (Figure 3I). Good expanders demonstrated enrichment of RUNX3, a TF known to inhibit Th2 lineage differentiation and increase Th1 effector molecules, such as IFNG.[37] RUNX3 overexpression is also associated with downregulation of ApoE and CCL2 immune-suppressive programs in myeloid cells.[38] In fact, the apheresis epigenetic landscape demonstrated myeloid signatures across both good and poor expanders, including IRF3, which is essential for the innate immune response,[39] Ets2, which drives myeloid suppressive populations,[40] and KLF6, which regulates macrophage polarization[41] (Figure 3I). In poor expanders, Gli1 was enriched, which is implicated in the regulation of inflammation and involved in the CD47-SIRPa pathway.[42] Given the crucial role that myeloid cells play in orchestrating immune responses and a growing body of literature that myeloid cells can limit immune responses in solid tumors,[43] we sought to robustly characterize the myeloid populations in patients receiving GD2 CAR-T therapy.

Myeloid cell populations in apheresis are associated with CAR-T expansion

We evaluated apheresis and post-treatment patient samples for potential myeloid contributors to CAR-T expansion. Phenotyping patient apheresis using an in-depth Myeloid CyTOF Panel demonstrated significantly reduced frequencies of monocytes and dendritic cells (DCs) in patients with good versus poor CAR-T expansion (Figure 4A). CIBERSORT RNA-seq analysis corroborated these findings that monocytes were associated with poor CAR-T expansion (Figure 4B). Using previously published datasets that characterized myeloid populations in the setting of cancer, we found that poor responders had increased gene signatures associated with CD16 monocytes[44] and myeloid-derived suppressor cells (MDSCs),[45–47] which was validated by surface phenotyping (Figures 4C and 4D). Further, apheresis samples of patients with poor CAR-T expansion enriched for a gene signature similar to that of monocytes from non-responders to PD-L1 inhibition,[48] suggesting a monocyte phenotype that limits other immunotherapeutic approaches beyond CAR-Ts (Figure 4C). GSEA indicated that samples from patients with poor CAR-T expansion were enriched in pathways associated with myeloid cell immune suppression in response to strong activation, such as LPS and TREM1-mediated phenotypes,[49] in parallel with reduced adaptive T and B cell immune signatures relative to myeloid populations, suggesting myeloid skewing in the circulating immune milieu (Figure 4E). These findings are consistent with observations that myeloid cells demonstrate marked plasticity, and by integrating signals from multiple stimuli can strongly modulate the T cell compartment and tailor the immune response.[50]

To further study the monocyte and DC populations, we performed a sub-clustering analysis of the myeloid populations at apheresis (Figures 5A, S5A, and S5B). CXCR3^{+} and CXCR3^{hi} classical monocytes, as well as CXCR3^{+}Slan^{+} and CXCR3^{+} Slan^{-} non-classical monocytes (nMo: CD14^{-}CD16^{+}), were significantly increased in good expanders; meanwhile, CXCR3^{-} classical monocytes (cMo: CD14^{+}CD16^{-}) and both clusters of intermediate monocytes (iMo: CD14^{dim}CD16^{+}) were significantly increased in poor expanders (Figure 5A). Overall, non-classical CXCR3^{+} monocytes correlated positively with CAR-T expansion, while CXCR3^{-} classical and intermediate (iMo2) monocyte populations negatively correlated with CAR-T expansion (Figure S5C). Pseudotime trajectory analysis demonstrated progression from classical to intermediate to non-classical monocytes and from CXCR3^{-} to CXCR3^{+} populations, suggesting that poor CAR-T expanders displayed a less-differentiated monocyte phenotype (Figures S5D and S5E). Multidimensional scaling of these samples demonstrated that patients with poor expansion cluster together, indicating commonalities in the apheresis of poor expanders, while good expanders have more diversity (Figure 5B). In agreement with the T cell Phenotype Panel analyses, the Myeloid Panel analyses identified that patients with good CAR-T expansion had increased expression of CCR7, CD45RA, and GITR/CD357 prior to CAR-T manufacturing (Figure 5C). Random forest analysis showed that CXCR3 on myeloid cells is the most important feature distinguishing good CAR-T expansion from poor CAR-T expansion (Figure 5D). In contrast, patients who experienced poor CAR-T cell expansion had increased myeloid expression of the canonical monocyte markers CD11b and CD14, the MDSC marker CD33, which mirrors pathways observed in the transcriptomic analyses and metabolic dearrangements reported in MDSCs (Figure 5C).[44–46,48,49]

Post-treatment patient sample characterization suggests myeloid molecular signatures associate with poor CAR-T expansion and persistence

Extending beyond differences of myeloid populations prior to treatment that could contribute to CAR-T expansion, we interrogated whether myeloid populations changed in response to CAR-T administration. Consistent with previous reports,[11] complete blood count analysis showed that the absolute monocyte count was significantly increased in poor CAR-T expanders 2 weeks after treatment relative to those patients with good CAR-T expansion (Figure 6A). Cytokine analysis indicated that good expanders had increased plasma levels of GM-CSF and IL-12, which are associated with monocyte differentiation and antitumor responses, respectively (Figure 6B). Moreover, post-treatment IL-12 strongly associated with the presence of CXCR3^{+} myeloid populations (Figure S6A). Myeloid Panel CyTOF analysis of peripheral blood immune populations showed significant increases in CXCR3^{-} cMo and iMo2 clusters, with a significant decrease in the CXCR3^{hi} cMo cluster, following CAR-T cell infusion (Figures 6C and 6D). Of note, poor expanders did not have differences in their monocyte populations pre- versus post-treatment, while the good expanders had

(E) The Activation Score based on Panther dataset. The Exhaustion Score was based on dataset of a previously described CAR-T model of exhaustion.[29] Boxplot represents all patients (dots) with median (line) and range (whiskers). Statistical analysis conducted by Mann-Whitney test (n = 8 patients).
(F) Volcano plot of CAR-T products demonstrates 60 chromatin features higher in accessibility in good or poor expanders based on FDR-adjusted p value ≤ 0.05 and log2FC > 2 (n = 11 patients).
(G) Open transcription factor motifs identified by combination of log(qvalue) and odds ratio (n = 11 patients). Also see Figures S3, S4, and Table S2.

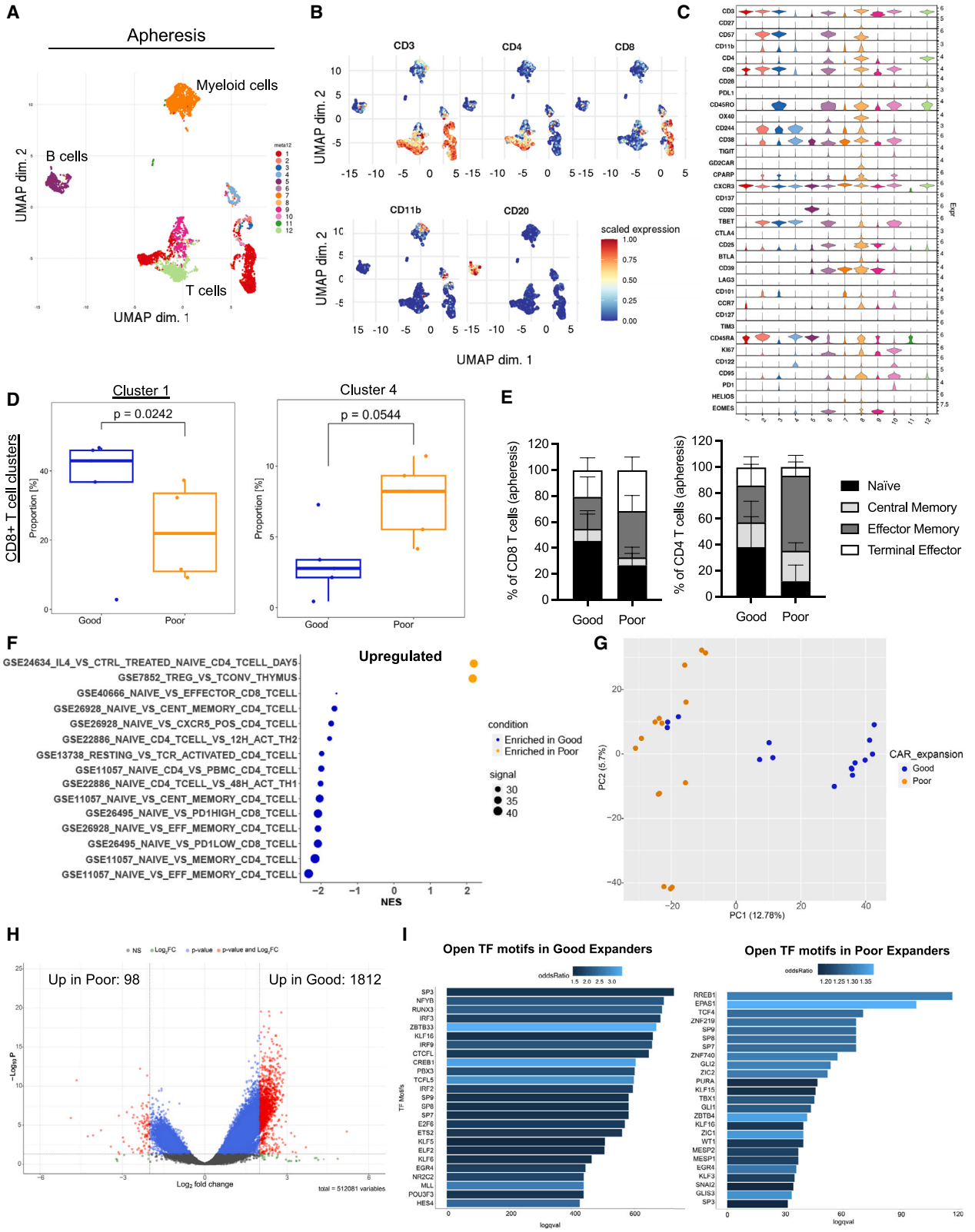

Figure 3. Apheresis memory T cell signatures correlate with CAR-T expansion in patients

(A) UMAP clusters of immune cell populations in apheresis from the T cell Phenotype CyTOF Panel (n = 10 patients).

(B) Median marker gene expression in populations in apheresis from the T cell Phenotype CyTOF Panel (n = 10 patients).

(legend continued on next page)

monocyte populations that shifted from a favorable pre-treatment phenotype to a phenotype that resembles the poor expanders following CAR-T treatment (Figure 6D). In fact, this shift was consistent when evaluating CXCR3 expression on all myeloid cells (Figure 6E). These data suggest that the CXCR3^{-} monocyte population associated with poor CAR-T expansion may also be responsible for limited CAR-T persistence in patients who experienced good initial CAR-T expansion.

Given CXCR3 expression may represent a marker of an activated immune response, we explored CXCR3 expression in other inflammatory settings. We identified a trend of higher CXCR3 expression in monocytes of hospitalized COVID-19 patients as compared to those not hospitalized,[51] suggesting increased immune activation in these patients (Figure 6F). As CXCR3 expression was the most significant indicator of CAR-T expansion in our patients, we queried the TARGET-OS dataset[52] and found that high CXCR3 expression was associated with significantly increased survival in patients with osteosarcoma; conversely, low CXCR3 expression was associated with reduced survival (Figures 6G, S6B, and S6C). Together, these data demonstrate that monocyte populations, specifically CXCR3^{+} or CXCR3^{hi} classical monocytes, are associated with good CAR-T expansion in patients and provide evidence for a T cell-extrinsic, monocyte-dependent mechanism contributing to CAR-T efficacy.

To begin to understand interactions of these myeloid populations and T cell populations, we tested whether direct interaction of CXCR3-expressing monocytes with GD2 CAR-Ts would have an impact on CAR-T function. Given CXCR3 expression can be induced by interferon signaling, and immune cells produce interferon upon activation, we investigated whether interferons could be predominantly responsible for the upregulation of CXCR3 on primary human monocytes. Exposure to neither recombinant interferon alpha (IFN α) nor interferon gamma (IFN γ) *in vitro* significantly altered CXCR3 expression on primary human monocytes from three healthy donors or the THP-1 monocyte cell line, suggesting multiple CXCR3 ligands beyond IFNs may be at play in the *in vivo* tumor microenvironment setting (Figure S6D). Further, we established a stable CXCR3-expressing THP-1 (CXCR3^{+} THP-1) cell line by viral transduction (Figure S6E) and co-cultured these CXCR3^{+} THP-1 cells or untransduced THP-1 (UTD THP-1) cells with GD2 CAR-Ts in the presence of GD2^{+} 143B osteosarcoma tumor cells. UTD THP-1 cells cultured with GD2 CAR-Ts and 143B tumor cells reduced IFNγ production by GD2 CAR-Ts, while co-culture with CXCR3^{+} THP-1 cells maintained IFN γ production (Figure S6F). These data suggest CXCR3 expression on monocytes can impact CAR-T function, underscoring an area of great interest and continued investigation.

DISCUSSION

Here, we report on a Phase I trial of a third-generation GD2 CAR-T therapy for GD2^{+} solid tumor in pediatric and young adult patients with osteosarcoma and neuroblastoma. This trial met its primary objectives with successful manufacturing of CAR-Ts from fifteen patients and safe administration of GD2 CAR-Ts to eleven patients with osteosarcoma and two with neuroblastoma.

Despite all patients on study eventually experiencing disease progression, a portion of patients exhibited GD2 CAR-T expansion similar to that seen in clinically active leukemia patient CAR-T trials.[25–27] Although there were no objective responses, three patients had stable disease beyond day 90 and all three had good CAR-T expansion. Therefore, we performed multi-dimensional correlative studies on pre-treatment apheresis, CAR-T product, and post-infusion peripheral blood patient samples to identify central mechanisms of CAR-T expansion and explore immune mediators of CAR-T persistence and efficacy.

While the causes of inadequate CAR-T expansion in solid tumors are likely multifactorial, experience in preclinical models and hematologic malignancies suggests that T cell exhaustion and inadequate memory potentially play an integral role.[53] In this study, we demonstrate that increased baseline naïve T cell subsets are associated with good CAR-T expansion. These findings align with studies showing early memory T cells in pre-manufacturing apheresis as a biomarker of CAR-T success in pediatric acute lymphoblastic leukemia[14,54] and chronic lymphocytic leukemia.[15] Single-cell RNA-seq analyses of CD19 CAR-T products from lymphoma patients also found the presence of memory T cells to be associated with good clinical response.[17] Our study expands these discoveries to solid tumors, where a favorable T cell population prior to CAR-T manufacturing could enhance CAR-T activity. Suppressive T cell populations may also contribute to poor CAR-T activity, as evidenced by elevation of Helios protein expression in post-treatment time points, suggesting regulatory T cells contributing to poor CAR-T functionality, in line with recent identification of these populations in CD19 CAR-T-treated patients.[34,35] Finally, our patients demonstrated exhaustion signatures that may explain the inability of CAR-Ts to persist. This observation was present across all patient product samples with exhaustion significantly increasing in the context of manufacturing and may help explain lack of efficacy observed. These patient findings confirm previous preclinical models of GD2 CAR-Ts showing tonic signaling and exhaustion as a limitation of CAR-T activity,[19] and highlight the potential benefit of incorporating approaches to reduce tonic signaling and exhaustion, such as with use of dasatinib in preclinical models[55] and in new GD2 CAR-T clinical trials[22] (NCT04539366 and

(C) Violin plots of marker expression levels in each cell cluster from the T cell Phenotype CyTOF Panel (n = 10 patients).
(D) Difference in proportion of cells in cluster 1 and cluster 4 in good versus poor expanders. Boxplot represents all patients (dots) with median (line) and range (whiskers). Statistical calculations by generalized linear mixed model. p values calculated as FDR-adjusted p values (n = 10 patients).
(E) CyTOF manual gating characterization of memory CD8 and CD4 T cell populations based on CD45RA and CCR7 (n = 10 patients).
(F) Selected C7 pathways significantly enriched in the transcriptome of good versus poor expanders (n = 10 patients). Statistical analysis calculated by Wilcoxon rank-sum test.
(G) Principal component analysis (PCA) plot of patient samples analyzed by ATAC-seq colored by expansion (blue = good; orange = poor) (n = 11 patients).
(H) Volcano plot of CAR-T products demonstrate 60 chromatin features up higher in accessibility in good or poor based on FDR-adjusted p value $\leq$ 0.05 and log2FC > 2 (n = 11 patients).
(I) Open transcription factor motifs identified by combination of log(qvalue) and odds ratio (n = 11 patients). Also see Figures S3 and S4.

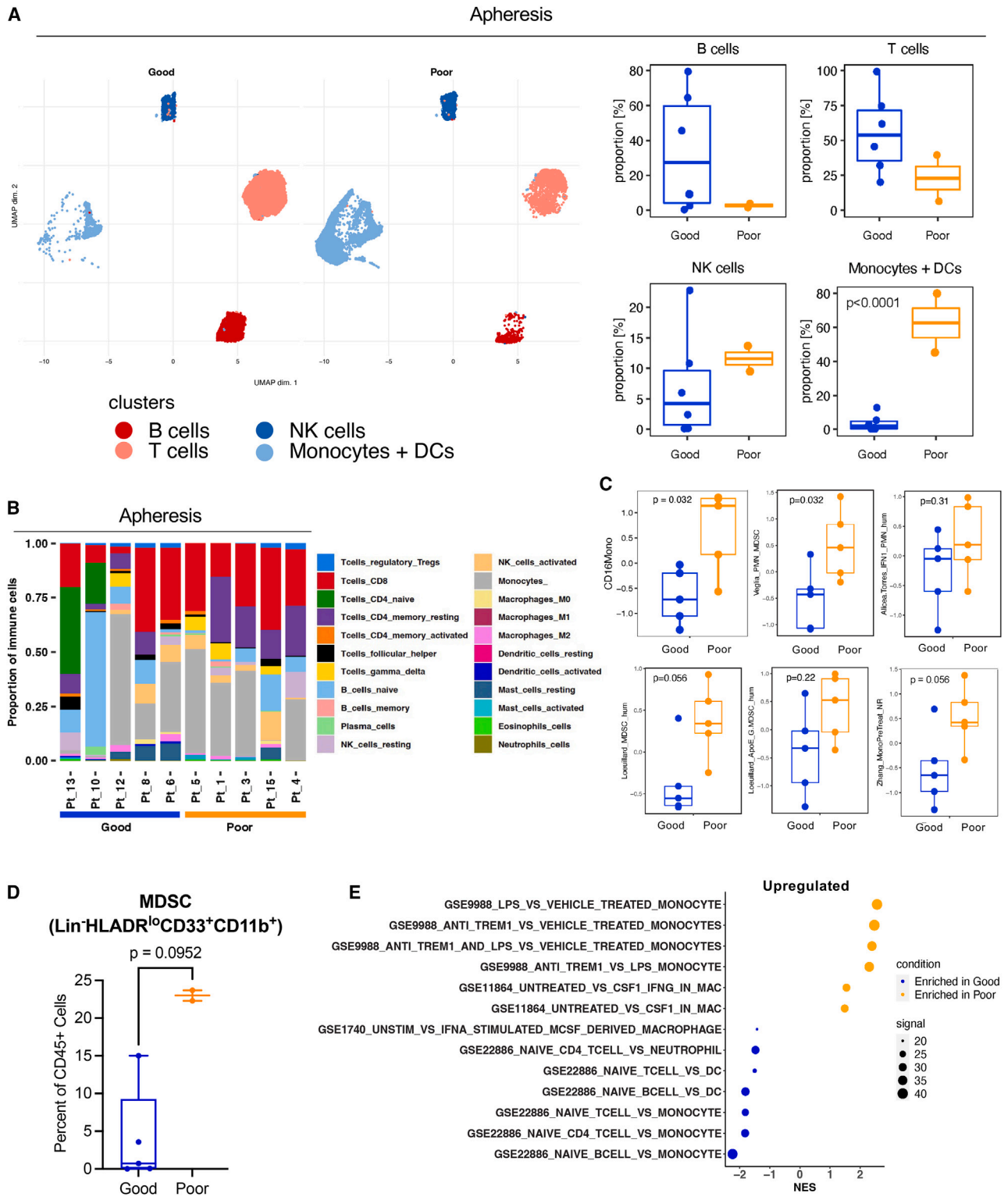

Figure 4. Apheresis myeloid cells and myeloid cell activation programs are associated with poor CAR-T expansion

(A) UMAP clusters and boxplots of immune cell populations in apheresis from the Myeloid CyTOF Panel. Boxplot represents all patients (dots) with median (line) and range (whiskers). Statistical calculations by generalized linear mixed model. p values calculated as FDR-adjusted p values (n = 8).

(B) Stacked bar plots of CIBERSORT data from RNA-seq analysis delimitating predicted immune cell composition in apheresis (n = 10 patients).

(C) Enriched gene signatures stratified by CAR-T expansion. Boxplot represents all patients (dots) with median (line) and range (whiskers). Statistical calculations by FDR-adjusted p value (n = 10 patients).

(legend continued on next page)

NCT04196413). Identifying these T cell phenotypes that correlate with CAR-T expansions provides an opportunity to understand the mechanisms of CAR-T failure and craft approaches to improve CAR-T activity.

While most CAR-T studies have focused exclusively on T cell populations, our study extensively evaluates myeloid cell subsets as they relate to CAR-T expansion. Our transcriptomic analysis identified elevated MDSC signatures in the apheresis of patients who went on to experience poor CAR-T expansion, a population that, when targeted, can improve CAR-T activity in solid tumor mouse models.[56] Further, GSEA points to an inflammatory activation of monocyte populations in poor expanders, with enrichment of lymphocytes over myeloid cell programs in good expanders. Using high-dimensional proteomic profiling of myeloid populations, we identified that classical monocytes were significantly elevated in the pre-treatment apheresis of patients with poor CAR-T expansion, while non-classical monocytes were significantly increased in good expanders. The contribution of monocyte subsets in cancer progression has not been well defined to date. A key finding of our work is the identification of CXCR3 expression on monocytes at baseline as the most important feature associated with good CAR-T cell expansion. This $CXCR3^{+}$ monocyte population was reduced post CAR-T therapy in parallel with loss of CAR-T persistence, suggesting that the myeloid program has marked plasticity and can modulate changes in T cell activation states and other inflammatory cues. Our findings were validated in TARGET-OS patient data, where high CXCR3 expression was associated with a survival benefit in osteosarcoma patients as well as other malignancies. CXCR3 has been extensively studied on T cells, but its function on myeloid populations is yet to be fully explored, with contradictory evidence reported in the literature of both pro-tumorigenic and antitumor functions.[57–59] Preliminary mechanistic *in vitro* studies suggest that CXCR3 expression on monocytes can maintain CAR-T functionality, but CAR-T IFN γ production is reduced by monocytes not expressing CXCR3. Further work is needed to understand the CXCR3 signaling pathway in myeloid cells and its modulation in the CAR-T immunotherapy setting. The results of our study demonstrate that the peripheral immune environment, in particular, the myeloid milieu prior to CAR-T administration, may effectively predict and modulate CAR-T expansion in patients. Further, patients with poor CAR-T expansion had significantly elevated absolute monocyte counts in circulation following CAR-T administration, indicating that monocytes are expanding in response to treatment and may be a central factor limiting CAR-T persistence. When expanded to brain tumor immunotherapy, myeloid populations appear to similarly dictate CAR-T expansion, cytokine kinetics, and activity.[22] These findings deepen our biological understanding of myeloid population kinetics and contributions to immunotherapy outcomes.

As the use of CAR-Ts expands beyond hematologic malignancies, it is imperative to perform in depth reverse translational evaluations to identify mediators of CAR-T efficacy in solid and brain tumors. The main limitation of this pediatric solid tumor trial is the small study size, which is a function of the relatively small total number of eligible patients with osteosarcoma or neuroblastoma with metastatic or relapsed refractory disease,[60,61] a reflection of the log-fold lower scale of pediatric oncology to adult oncology. The patients represented in this study are consistent with the majority of patients in pediatric and adult relapsed, refractory solid tumor Phase I studies, where patients tend to be diverse in tumor type, disease burden, and baseline progression rate. We have developed a disease burden assessment score (Table 2), and this score trended with our AI-generated disease burden quantification (Table 3), which provides a mechanism for comparing heterogeneous early phase clinical trial patients in this and future work. In light of the limitations of small study size and diversity in disease burden, the statistical significance of our key findings underscores their biological importance and provides a starting point and motivation for validation in subsequent studies.

The comprehensive correlative analyses that we performed can serve as a roadmap for cell therapy clinical trial correlative studies. Understanding the T and myeloid cell molecular drivers of CAR-T expansion in solid tumor patients will aid in the identification of modifiable pathways to improve CAR-T efficacy for patients and opens the door for the addition of myeloid-based interventions.

STAR★METHODS

Detailed methods are provided in the online version of this paper and include the following:

- KEY RESOURCES TABLE
- RESOURCE AVAILABILITY
  - Lead contact
  - Materials availability
  - Data and code availability
- EXPERIMENTAL MODEL AND STUDY PARTICIPANT DETAILS
  - Trial design
- METHOD DETAILS
  - CAR-T Cell manufacturing
  - Cytokine assay
  - qPCR assay
  - Mass cytometry, cytometry by time of flight (CyTOF), assay and analysis
  - RNA-sequencing assay and analysis
  - ATAC-seq assay and analysis
  - Primary monocyte assays
  - Cell lines
  - Co-culture assays
  - Disease burden assessments
- QUANTIFICATION AND STATISTICAL ANALYSIS
  - CyTOF analysis
  - RNA-seq analysis

(D) Flow cytometry analysis of Myeloid-Derived Suppressor Cell (MDSC) phenotype in patients' pre-treatment apheresis samples (n = 9). Statistical analysis calculated by Mann-Whitney test.
(E) Selected C7 myeloid pathways significantly enriched in poor expanders compared to good expanders (n = 10 patients). Statistical analysis calculated by Wilcoxon rank-sum test.

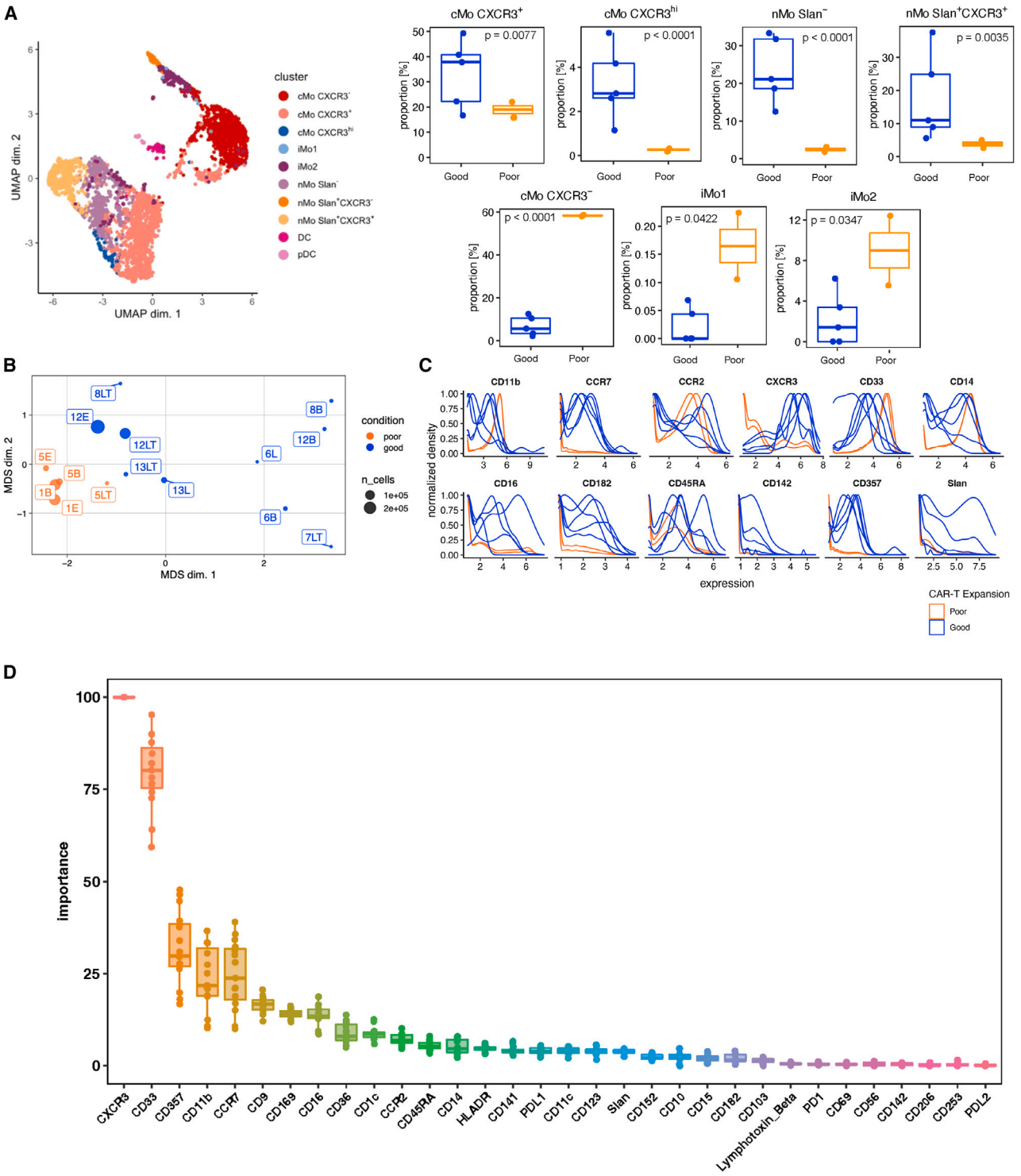

Figure 5. Apheresis CXCR3 expression on monocytes is a marker of good CAR-T expansion

(A) UMAP clusters and boxplots (median and range) of myeloid cell subpopulations in apheresis from the Myeloid CyTOF Panel. Boxplot represents all patients (dots) with median (line) and range (whiskers). Statistical calculations by generalized linear mixed model. p values calculated as FDR-adjusted p values (n = 7 patients).

(B) MDS plots of myeloid cell subpopulations in apheresis labeled by patient and colored by expansion (blue = good expansion; orange = poor expansion) (n = 7 patients).

(C) Density plots showing expression of select markers (blue = good expansion; orange = poor expansion) (n = 7 patients).

(D) Boxplot of importance scores from 30 iterations of random forest analysis depicting the strength of association of markers with CAR-T expansion and representative CyTOF expression plots. Markers are sorted by average importance scores. Boxplot represents all iterations (dots) with median (line) and range (whiskers) (n = 7 patients). Also see Figure S5.

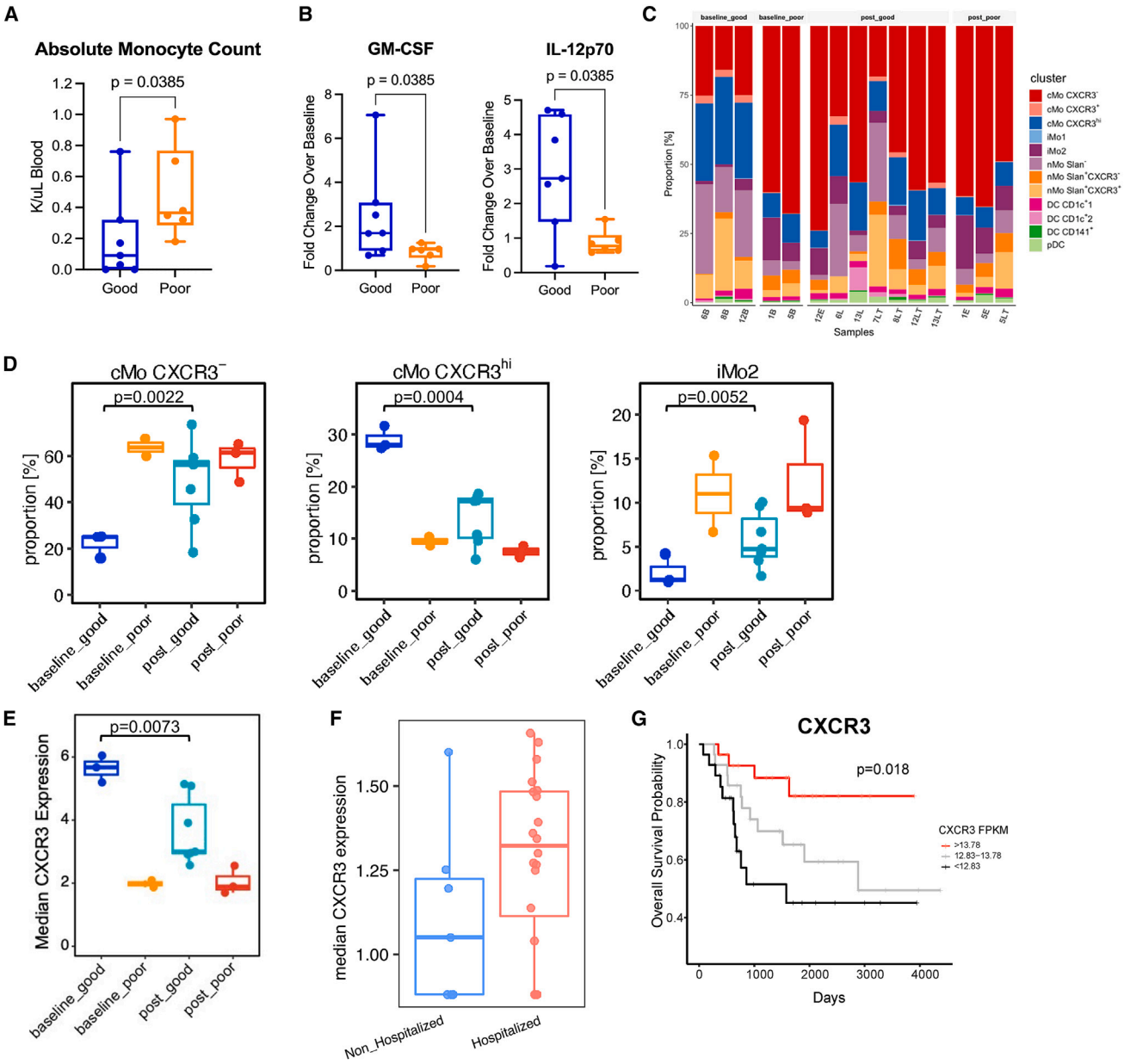

Figure 6. Myeloid populations shift in response to CAR-T treatment

(A) Absolute monocyte count in peripheral blood 14 ± 3 days post CAR-T infusion. Boxplot represents all patients (dots) with median (line) and range (whiskers). Statistical analysis by Mann-Whitney test (n = 13).

(B) Protein levels of GM-CSF and IL-12p70 in the plasma of patients 7–14 days and 25–27 days following CAR-T administration, respectively. Boxplot represents all patients (dots) with median (line) and range (whiskers). Statistical analysis by Mann-Whitney test (n = 13).

(C) Stacked bar plots of patient samples by cluster from the Myeloid CyTOF Panel (n = 7 patients).

(D) Boxplots of immune cell populations in pre- and post-treatment samples from the Myeloid CyTOF Panel. Boxplot represents all patients (dots) with median (line) and range (whiskers). Statistical calculations by generalized linear mixed model. p values calculated as FDR-adjusted p values (n = 7 patients).

(E) Boxplot of CXCR3 expression on myeloid cells in pre- and post-treatment samples from the Myeloid CyTOF Panel. Boxplot represents all patients (dots) with median (line) and range (whiskers). Statistical calculations by linear mixed model. p values calculated as FDR-adjusted p values (n = 7 patients).

(F) CXCR3 expression on myeloid cells in patients hospitalized versus not hospitalized with COVID-19. Boxplot represents all patients (dots) with median (line) and range (whiskers). Statistical calculations by linear mixed model. p value calculated as FDR-adjusted p value (p = 0.117; n = 27 patients).

(G) Overall survival of patients in TARGET-OS dataset stratified by expression level of CXCR3. Statistical analysis on group survival differences was performed utilizing the log rank test. Also see Supplemental Figure S5 and S6.

- Expression analysis on publicly available datasets
- ATAC-seq analysis

- ADDITIONAL RESOURCES

SUPPLEMENTAL INFORMATION

Supplemental information can be found online at https://doi.org/10.1016/j.ccell.2023.11.011.

ACKNOWLEDGMENTS

We are grateful to the study participants and their families, referring medical care teams, the faculty and staff of the NIH, and the data managers involved with this work. The clinical trial was supported in part by the Intramural Research Program, the National Cancer Institute, NIH Clinical Center, and the National Institutes of Health (NIH NCI ZIABC011332-06 and NIH NCI ZIABC011334-10 to R.N.K.). Scientific and financial support for the Cancer Immune Monitoring and Analysis Centers - Cancer Immunologic Data Commons (CIMAC-CIDC) Network are provided through the National Cancer Institute (NCI) Cooperative Agreements: U24CA224331 (to the Dana-Farber Cancer Institute CIMAC), U24CA224309 (to the Stanford University CIMAC), and U24CA224316 (to the CIDC at Dana-Farber Cancer Institute). The myeloid analyses presented in this study were supported in part by NCI U01 CA224766 (to C.C.H., R.N.K., and D.S.) and NCI R01 CA202987 (to C.C.H.). C.F.C. was supported by the NIH Oxford-Cambridge Scholars Program and the Center for Cancer Research Center for Cell-based Therapy Cancer Moonshot Initiative. Scientific and financial support for the Partnership for Accelerating Cancer Therapies (PACT) public-private partnership (PPP) are made possible through funding support provided to the FNIH by AbbVie, Amgen, Boehringer-Ingelheim Pharma GmbH & Co. KG, Bristol-Myers Squibb, Celgene Corporation, Genentech, Gilead, GlaxoSmithKline plc, Janssen Pharmaceutical Companies of Johnson & Johnson, Novartis Institutes for Biomedical Research, Pfizer, and Sanofi. T.M. received support from the Stanford Medical Scientist Training Program grant T32GM007365, the NCI under Award Number F30CA271797, the Stanford Interdisciplinary Graduate Fellowship, and the Stanford ChEM-H Chemistry/Biology Interface Predoctoral Training Program and the Stanford ChEM-H O'Leary-Thiry Graduate Fellowship. We also thank Sam Pollock, Hayley Lyon, Srin Ranasinghe, project managers of the Broad Institute genomics platform, and DFCI and the Childhood Cancer Data Initiative team in the intramural research program, National Cancer Institute. Some of the computing for this project was performed on the Sherlock cluster. We would like to thank Stanford University and the Stanford Research Computing Center for providing computational resources and support that contributed to these research results. Graphical abstract and schematics in figures were created with BioRender.com.

AUTHOR CONTRIBUTIONS

S.R. and R.N.K. conceived the project. C.L.M. and R.N.K. were the principal investigators of the trial. S.R., R.N.K., and C.C.H. designed the correlative studies. S.K., T.M., A.A., C.C.H., S.R., and R.N.K. generated, edited, and oversaw all the figures. D.B., A.C., J.D., M.M., J.G., C.L.M., and R.N.K. designed, performed, analyzed all patient clinical and radiographic data, and supervised clinical trial. T.M., C.D., P.B.S., B.S., S.B., H.M., C.L.M., S.R., and R.N.K. performed and analyzed all the T cell CyTOF studies. S.K., A.A., C.F.C., N.A.G., C.C.H., S.R., and R.N.K. performed and analyzed all the myeloid cell CyTOF studies. S.K., T.M., A.A., C.F.C., J.A., Y.L., A.J., V.D., H.A., C.C.H., S.R., and R.N.K. designed, performed, and analyzed the RNA-seq-related studies. T.M. and A.A. conducted random forest AI analyses. S.K., C.F.C., and C.O. generated the CXCR3+ THP-1 cell line. S.A.H. and T.B. performed the quantitative AI-assisted total lesion glycolysis score. J.K.-S., J.E.S., E.D., and R.N.K. developed the tumor burden assessment score and analyzed the patient clinical and radiographic data to score each patient. T.M., W.R., R.B., E.S., B.S., C.L.M., and S.R. performed and analyzed all the ATAC sequencing. M.P., S.B., H.M., C.L.M., S.R., and R.N.K. secured funding for CyTOF, ATAC-seq, and RNA-seq assays. S.K., T.M., A.A., C.F.C., C.D., P.B.S., W.R., N.A.G., R.B., J.A., Y.L., A.J., V.D., H.A., C.O., H.Z., R.M., J.Y., R.B., S.V.N., J.L., M.P., E.S., J.K.-S., J.E.S., E.D., S.A.H., B.T., B.S., S.B., H.M., S.L.H., F.N.G., C.C.H., S.R., and R.N.K. performed the experiments and analyzed the data. S.K., T.M., A.A., C.F.C., C.D., W.R., N.A.G., R.B., C.J.W., F.M., J.A., Y.L., A.J., V.D., H.A., C.O., E.S., J.K.-S., J.E.S., E.D., S.A.M., B.S., S.B., H.M., S.L.H., M.M., C.C.H., C.L.M., S.R., and R.N.K. wrote or edited the manuscript.

DECLARATION OF INTERESTS

C.J.W. receives research funding from Pharmacyclics and hold equity in BioNTech, Inc. F.M. is a cofounder of and has equity in Harbinger Health, has equity in Zephyr AI, and serves as a consultant for Harbinger Health, Zephyr AI, and Red Cell Partners and Exscientia. F.M. declares that none of these relationships are directly or indirectly related to the content of this manuscript. E.S. consults for and holds equity in Lyell Immunopharma and consults for Lepton Pharmaceuticals and Galaria. M.S.M. is currently employed at Normunity and holds stock in AstraZeneca; her contributions to this work were made prior to these industry positions which are not relevant to the content of this manuscript. C.L.M. is an inventor on numerous patents and patents pending related to CAR-T cell therapies. C.L.M. holds equity in and receives research funding from Lyell Immunopharma and holds equity in and consults for CARGO Therapeutics and Link Cell Therapies. C.L.M. consults for Immatics, Mammoth, Ensoma, and Red Tree Venture Capital.

INCLUSION AND DIVERSITY

We support inclusive, diverse, and equitable conduct of research. One or more of the authors of this paper self-identifies as an underrepresented ethnic minority in their field of research or within their geographical location. One or more of the authors of this paper self-identifies as a gender minority in their field of research. One or more of the authors of this paper received support from a program designed to increase minority representation in their field of research. One or more of the authors of this paper self-identifies as a member of the LGBTQIA+ community.

Received: January 10, 2023
Revised: September 18, 2023
Accepted: November 22, 2023
Published: December 21, 2023

REFERENCES

1. Louis, D.N., Perry, A., Reifenberger, G., von Deimling, A., Figarella-Branger, D., Cavenee, W.K., Ohgaki, H., Wiestler, O.D., Kleihues, P., and Ellison, D.W. (2016). The 2016 World Health Organization Classification of Tumors of the Central Nervous System: a summary. Acta Neuropathol. *131*, 803–820.
2. Perkins, S.M., Shinohara, E.T., DeWees, T., and Frangoul, H. (2014). Outcome for children with metastatic solid tumors over the last four decades. PLoS One *9*, e100396.
3. Ceschel, S., Casotto, V., Valsecchi, M.G., Tamaro, P., Jankovic, M., Hanau, G., Fossati, F., Pillon, M., Rondelli, R., Sandri, A., et al. (2006). Survival after relapse in children with solid tumors: a follow-up study from the Italian off-therapy registry. Pediatr. Blood Cancer *47*, 560–566.
4. Meyers, P.A., Schwartz, C.L., Krailo, M.D., Healey, J.H., Bernstein, M.L., Betcher, D., Ferguson, W.S., Gebhardt, M.C., Goorin, A.M., Harris, M., et al. (2008). Osteosarcoma: the addition of muramyl tripeptide to chemotherapy improves overall survival–a report from the Children's Oncology Group. J. Clin. Oncol. *26*, 633–638.
5. Cooney, T., Lane, A., Bartels, U., Bouffet, E., Goldman, S., Leary, S.E.S., Foreman, N.K., Packer, R.J., Broniscer, A., Minturn, J.E., et al. (2017). Contemporary survival endpoints: an International Diffuse Intrinsic Pontine Glioma Registry study. Neuro Oncol. *19*, 1279–1280.
6. Fisher, P.G., Breiter, S.N., Carson, B.S., Wharam, M.D., Williams, J.A., Weingart, J.D., Foer, D.R., Goldthwaite, P.T., Tihan, T., and Burger, P.C. (2000). A clinicopathologic reappraisal of brain stem tumor classification. Identification of pilocystic astrocytoma and fibrillary astrocytoma as distinct entities. Cancer *89*, 1569–1576.

7. Chou, A.J., Merola, P.R., Wexler, L.H., Gorlick, R.G., Vyas, Y.M., Healey, J.H., LaQuaglia, M.P., Huvos, A.G., and Meyers, P.A. (2005). Treatment of osteosarcoma at first recurrence after contemporary therapy: the Memorial Sloan-Kettering Cancer Center experience. Cancer *104*, 2214–2221.
8. Yu, A.L., Gilman, A.L., Ozkaynak, M.F., London, W.B., Kreissman, S.G., Chen, H.X., Smith, M., Anderson, B., Villablanca, J.G., Matthay, K.K., et al. (2010). Anti-GD2 antibody with GM-CSF, interleukin-2, and isotretinoin for neuroblastoma. N. Engl. J. Med. *363*, 1324–1334.
9. Pule, M.A., Savoldo, B., Myers, G.D., Rossig, C., Russell, H.V., Dotti, G., Huls, M.H., Liu, E., Gee, A.P., Mei, Z., et al. (2008). Virus-specific T cells engineered to coexpress tumor-specific receptors: persistence and antitumor activity in individuals with neuroblastoma. Nat. Med. *14*, 1264–1270.
10. Louis, C.U., Savoldo, B., Dotti, G., Pule, M., Yvon, E., Myers, G.D., Rossig, C., Russell, H.V., Diouf, O., Liu, E., et al. (2011). Antitumor activity and long-term fate of chimeric antigen receptor-positive T cells in patients with neuroblastoma. Blood *118*, 6050–6056.
11. Heczey, A., Louis, C.U., Savoldo, B., Dakhova, O., Durett, A., Grilley, B., Liu, H., Wu, M.F., Mei, Z., Gee, A., et al. (2017). CAR T Cells Administered in Combination with Lymphodepletion and PD-1 Inhibition to Patients with Neuroblastoma. Mol. Ther. *25*, 2214–2224.
12. Del Bufalo, F., De Angelis, B., Caruana, I., Del Baldo, G., De Ioris, M.A., Serra, A., Mastronuzzi, A., Cefalo, M.G., Pagliara, D., Amicucci, M., et al. (2023). GD2-CART01 for Relapsed or Refractory High-Risk Neuroblastoma. N. Engl. J. Med. *388*, 1284–1295.
13. Porter, D.L., Hwang, W.T., Frey, N.V., Lacey, S.F., Shaw, P.A., Loren, A.W., Bagg, A., Marcucci, K.T., Shen, A., Gonzalez, V., et al. (2015). Chimeric antigen receptor T cells persist and induce sustained remissions in relapsed refractory chronic lymphocytic leukemia. Sci. Transl. Med. *7*, 303ra139.
14. Singh, N., Perazzelli, J., Grupp, S.A., and Barrett, D.M. (2016). Early memory phenotypes drive T cell proliferation in patients with pediatric malignancies. Sci. Transl. Med. *8*, 320ra3. 320ra323-320ra323.
15. Fraietta, J.A., Lacey, S.F., Orlando, E.J., Pruteanu-Malinici, I., Gohil, M., Lundh, S., Boesteanu, A.C., Wang, Y., O'Connor, R.S., Hwang, W.T., et al. (2018). Determinants of response and resistance to CD19 chimeric antigen receptor (CAR) T cell therapy of chronic lymphocytic leukemia. Nat. Med. *24*, 563–571.
16. Das, R.K., Vernau, L., Grupp, S.A., and Barrett, D.M. (2019). Naïve T-cell Deficits at Diagnosis and after Chemotherapy Impair Cell Therapy Potential in Pediatric Cancers. Cancer Discov. *9*, 492–499.
17. Deng, Q., Han, G., Puebla-Osorio, N., Ma, M.C.J., Strati, P., Chasen, B., Dai, E., Dang, M., Jain, N., Yang, H., et al. (2020). Characteristics of anti-CD19 CAR T cell infusion products associated with efficacy and toxicity in patients with large B cell lymphomas. Nat. Med. *26*, 1878–1887.
18. Finney, O.C., Brakke, H.M., Rawlings-Rhea, S., Hicks, R., Doolittle, D., Lopez, M., Futrell, R.B., Orentas, R.J., Li, D., Gardner, R.A., and Jensen, M.C. (2019). CD19 CAR T cell product and disease attributes predict leukemia remission durability. J. Clin. Invest. *129*, 2123–2132.
19. Long, A.H., Haso, W.M., Shern, J.F., Wanhainen, K.M., Murgai, M., Ingaramo, M., Smith, J.P., Walker, A.J., Kohler, M.E., Venkateshwara, V.R., et al. (2015). 4-1BB costimulation ameliorates T cell exhaustion induced by tonic signaling of chimeric antigen receptors. Nat. Med. *21*, 581–590.
20. Gargett, T., Yu, W., Dotti, G., Yvon, E.S., Christo, S.N., Hayball, J.D., Lewis, I.D., Brenner, M.K., and Brown, M.P. (2016). GD2-specific CAR T Cells Undergo Potent Activation and Deletion Following Antigen Encounter but can be Protected From Activation-induced Cell Death by PD-1 Blockade. Mol. Ther. *24*, 1135–1149.
21. Kaczanowska, S., Beury, D.W., Gopalan, V., Tycko, A.K., Qin, H., Clements, M.E., Drake, J., Nwanze, C., Murgai, M., Rae, Z., et al. (2021). Genetically engineered myeloid cells rebalance the core immune suppression program in metastasis. Cell *184*, 2033–2052.e21.
22. Majzner, R.G., Ramakrishna, S., Yeom, K.W., Patel, S., Chinnasamy, H., Schultz, L.M., Richards, R.M., Jiang, L., Barsan, V., Mancusi, R., et al. (2022). GD2-CAR T cell therapy for H3K27M-mutated diffuse midline gliomas. Nature *603*, 934–941.
23. Stroncek, D.F., Lee, D.W., Ren, J., Sabatino, M., Highfill, S., Khuu, H., Shah, N.N., Kaplan, R.N., Fry, T.J., and Mackall, C.L. (2017). Elutriated lymphocytes for manufacturing chimeric antigen receptor T cells. J. Transl. Med. *15*, 59.
24. Gyurdieva, A., Zajic, S., Chang, Y.-F., Houseman, E.A., Zhong, S., Kim, J., Nathenson, M., Faitg, T., Woessner, M., Turner, D.C., et al. (2022). Biomarker correlates with response to NY-ESO-1 TCR T cells in patients with synovial sarcoma. Nat. Commun. *13*, 5296.
25. Maude, S.L., Frey, N., Shaw, P.A., Aplenc, R., Barrett, D.M., Bunin, N.J., Chew, A., Gonzalez, V.E., Zheng, Z., Lacey, S.F., et al. (2014). Chimeric antigen receptor T cells for sustained remissions in leukemia. N. Engl. J. Med. *371*, 1507–1517.
26. Fry, T.J., Shah, N.N., Orentas, R.J., Stetler-Stevenson, M., Yuan, C.M., Ramakrishna, S., Wolters, P., Martin, S., Delbrook, C., Yates, B., et al. (2018). CD22-targeted CAR T cells induce remission in B-ALL that is naive or resistant to CD19-targeted CAR immunotherapy. Nat. Med. *24*, 20–28. https://www.nature.com/articles/nm.4441#supplementary-information.
27. Lee, D.W., Kochenderfer, J.N., Stetler-Stevenson, M., Cui, Y.K., Delbrook, C., Feldman, S.A., Fry, T.J., Orentas, R., Sabatino, M., Shah, N.N., et al. (2015). T cells expressing CD19 chimeric antigen receptors for acute lymphoblastic leukaemia in children and young adults: a phase 1 dose-escalation trial. Lancet *385*, 517–528.
28. Foster, B., Bagci, U., Mansoor, A., Xu, Z., and Mollura, D.J. (2014). A review on segmentation of positron emission tomography images. Comput. Biol. Med. *50*, 76–96.
29. Lynn, R.C., Weber, E.W., Sotillo, E., Gennert, D., Xu, P., Good, Z., Anbunathan, H., Lattin, J., Jones, R., Tieu, V., et al. (2019). c-Jun overexpression in CAR T cells induces exhaustion resistance. Nature *576*, 293–300.
30. Canale, F.P., Ramello, M.C., Núñez, N., Araujo Furlan, C.L., Bossio, S.N., Gorosito Serrán, M., Tosello Boari, J., Del Castillo, A., Ledesma, M., Sedlik, C., et al. (2018). CD39 Expression Defines Cell Exhaustion in Tumor-Infiltrating CD8(+) T Cells. Cancer Res. *78*, 115–128.
31. Gupta, P.K., Godec, J., Wolski, D., Adland, E., Yates, K., Pauken, K.E., Cosgrove, C., Ledderose, C., Junger, W.G., Robson, S.C., et al. (2015). CD39 Expression Identifies Terminally Exhausted CD8+ T Cells. PLoS Pathog. *11*, e1005177.
32. Thornton, A.M., Korty, P.E., Tran, D.Q., Wohlfert, E.A., Murray, P.E., Belkaid, Y., and Shevach, E.M. (2010). Expression of Helios, an Ikaros transcription factor family member, differentiates thymic-derived from peripherally induced Foxp3+ T regulatory cells. J. Immunol. *184*, 3433–3441.
33. Piedra-Quintero, Z.L., Wilson, Z., Nava, P., and Guerau-de-Arellano, M. (2020). CD38: An Immunomodulatory Molecule in Inflammation and Autoimmunity. Front. Immunol. *11*, 597959.
34. Good, Z., Spiegel, J.Y., Sahaf, B., Malipatlolla, M.B., Ehlinger, Z.J., Kurra, S., Desai, M.H., Reynolds, W.D., Wong Lin, A., Vandris, P., et al. (2022). Post-infusion CAR TReg cells identify patients resistant to CD19-CAR therapy. Nat. Med. *28*, 1860–1871.
35. Haradhvala, N.J., Leick, M.B., Maurer, K., Gohil, S.H., Larson, R.C., Yao, N., Gallagher, K.M.E., Katsis, K., Frigault, M.J., Southard, J., et al. (2022). Distinct cellular dynamics associated with response to CAR-T therapy for refractory B cell lymphoma. Nat. Med. *28*, 1848–1859.
36. Furmanski, A.L., Barbarulo, A., Solanki, A., Lau, C.I., Sahni, H., Saldana, J.I., D'Acquisto, F., and Crompton, T. (2015). The transcriptional activator Gli2 modulates T-cell receptor signalling through attenuation of AP-1 and NFκB activity. J. Cell Sci. *128*, 2085–2095.
37. Korinfskaya, S., Parameswaran, S., Weirauch, M.T., and Barski, A. (2021). Runx Transcription Factors in T Cells—What Is Beyond Thymic Development? Front. Immunol. *12*, 701924.
38. Menezes, A.C., Jones, R., Shrestha, A., Nicholson, R., Leckenby, A., Azevedo, A., Davies, S., Baker, S., Gilkes, A.F., Darley, R.L., and Tonks,

A. (2022). Increased expression of RUNX3 inhibits normal human myeloid development. Leukemia *36*, 1769–1780.

39. Tamura, T., Yanai, H., Savitsky, D., and Taniguchi, T. (2008). The IRF family transcription factors in immunity and oncogenesis. Annu. Rev. Immunol. *26*, 535–584.
40. Zabuawala, T., Taffany, D.A., Sharma, S.M., Merchant, A., Adair, B., Srinivasan, R., Rosol, T.J., Fernandez, S., Huang, K., Leone, G., and Ostrowski, M.C. (2010). An Ets2-Driven Transcriptional Program in Tumor-Associated Macrophages Promotes Tumor Metastasis. Cancer Res. *70*, 1323–1333.
41. Date, D., Das, R., Narla, G., Simon, D.I., Jain, M.K., and Mahabeleshwar, G.H. (2014). Kruppel-like Transcription Factor 6 Regulates Inflammatory Macrophage Polarization. J. Biol. Chem. *289*, 10318–10329.
42. Sheng, M., Lin, Y., Xu, D., Tian, Y., Zhan, Y., Li, C., Farmer, D.G., Kupiec-Weglinski, J.W., and Ke, B. (2021). CD47-Mediated Hedgehog/SMO/GLI1 Signaling Promotes Mesenchymal Stem Cell Immunomodulation in Mouse Liver Inflammation. Hepatology *74*, 1560–1577.
43. Mantovani, A., Marchesi, F., Jaillon, S., Garlanda, C., and Allavena, P. (2021). Tumor-associated myeloid cells: diversity and therapeutic targeting. Cell. Mol. Immunol. *18*, 566–578.
44. Mulder, K., Patel, A.A., Kong, W.T., Piot, C., Halitzki, E., Dunsmore, G., Khalilnezhad, S., Irac, S.E., Dubuisson, A., Chevrier, M., et al. (2021). Cross-tissue single-cell landscape of human monocytes and macrophages in health and disease. Immunity *54*, 1883–1900.e5.
45. Veglia, F., Hashimoto, A., Dweep, H., Sanseviero, E., De Leo, A., Tcyganov, E., Kossenkov, A., Mulligan, C., Nam, B., Masters, G., et al. (2021). Analysis of classical neutrophils and polymorphonuclear myeloid-derived suppressor cells in cancer patients and tumor-bearing mice. J. Exp. Med. *218*, e20201803.
46. Loeuillard, E., Yang, J., Buckarma, E., Wang, J., Liu, Y., Conboy, C., Pavelko, K.D., Li, Y., O'Brien, D., Wang, C., et al. (2020). Targeting tumor-associated macrophages and granulocytic myeloid-derived suppressor cells augments PD-1 blockade in cholangiocarcinoma. J. Clin. Invest. *130*, 5380–5396.
47. Alicea-Torres, K., Sanseviero, E., Gui, J., Chen, J., Veglia, F., Yu, Q., Donthireddy, L., Kossenkov, A., Lin, C., Fu, S., et al. (2021). Immune suppressive activity of myeloid-derived suppressor cells in cancer requires inactivation of the type I interferon pathway. Nat. Commun. *12*, 1717.
48. Zhang, Y., Chen, H., Mo, H., Hu, X., Gao, R., Zhao, Y., Liu, B., Niu, L., Sun, X., Yu, X., et al. (2021). Single-cell analyses reveal key immune cell subsets associated with response to PD-L1 blockade in triple-negative breast cancer. Cancer Cell *39*, 1578–1593.e8.
49. Dower, K., Ellis, D.K., Saraf, K., Jelinsky, S.A., and Lin, L.L. (2008). Innate immune responses to TREM-1 activation: overlap, divergence, and positive and negative cross-talk with bacterial lipopolysaccharide. J. Immunol. *180*, 3520–3534.
50. Bassler, K., Schulte-Schrepping, J., Warnat-Herresthal, S., Aschenbrenner, A.C., and Schultze, J.L. (2019). The Myeloid Cell Compartment—Cell by Cell. Annu. Rev. Immunol. *37*, 269–293.
51. Padgett, L.E., Dinh, H.Q., Chee, S.J., Olingy, C.E., Wu, R., Araujo, D.J., Vijayanand, P., Ottensmeier, C.H., and Hedrick, C.C. (2020). Interplay of Monocytes and T Lymphocytes in COVID-19 Severity. Preprint at bioRxiv. https://doi.org/10.1101/2020.07.17.209304.
52. Goldman, M.J., Craft, B., Hastie, M., Repečka, K., McDade, F., Kamath, A., Banerjee, A., Luo, Y., Rogers, D., Brooks, A.N., et al. (2020). Visualizing and interpreting cancer genomics data via the Xena platform. Nat. Biotechnol. *38*, 675–678.
53. Ramakrishna, S., Barsan, V., and Mackall, C. (2020). Prospects and challenges for use of CAR T cell therapies in solid tumors. Expet Opin. Biol. Ther. *20*, 503–516.
54. Chen, G.M., Chen, C., Das, R.K., Gao, P., Chen, C.H., Bandyopadhyay, S., Ding, Y.Y., Uzun, Y., Yu, W., Zhu, Q., et al. (2021). Integrative Bulk and Single-Cell Profiling of Premanufacture T-cell Populations Reveals Factors Mediating Long-Term Persistence of CAR T-cell Therapy. Cancer Discov. *11*, 2186–2199.
55. Weber, E.W., Parker, K.R., Sotillo, E., Lynn, R.C., Anbunathan, H., Lattin, J., Good, Z., Belk, J.A., Daniel, B., Klysz, D., et al. (2021). Transient rest restores functionality in exhausted CAR-T cells through epigenetic remodeling. Science *372*, eaba1786.
56. Long, A.H., Highfill, S.L., Cui, Y., Smith, J.P., Walker, A.J., Ramakrishna, S., El-Etriby, R., Galli, S., Tsokos, M.G., Orentas, R.J., and Mackall, C.L. (2016). Reduction of MDSCs with All-trans Retinoic Acid Improves CAR Therapy Efficacy for Sarcomas. Cancer Immunol. Res. *4*, 869–880.
57. Abron, J.D., Singh, N.P., Murphy, A.E., Mishra, M.K., Price, R.L., Nagarkatti, M., Nagarkatti, P.S., and Singh, U.P. (2018). Differential role of CXCR3 in inflammation and colorectal cancer. Oncotarget *9*, 17928–17936.
58. Butler, K.L., Clancy-Thompson, E., and Mullins, D.W. (2017). CXCR3+ monocytes/macrophages are required for establishment of pulmonary metastases. Sci. Rep. *7*, 45593.
59. Russo, E., Santoni, A., and Bernardini, G. (2020). Tumor inhibition or tumor promotion? The duplicity of CXCR3 in cancer. J. Leukoc. Biol. *108*, 673–685.
60. Liu, S., Yin, W., Lin, Y., Huang, S., Xue, S., Sun, G., and Wang, C. (2023). Metastasis pattern and prognosis in children with neuroblastoma. World J. Surg. Oncol. *21*, 130.
61. Tian, H., Cao, J., Li, B., Nice, E.C., Mao, H., Zhang, Y., and Huang, C. (2023). Managing the immune microenvironment of osteosarcoma: the outlook for osteosarcoma treatment. Bone Res. *11*, 11.
62. Good, Z., Sarno, J., Jager, A., Samusik, N., Aghaeepour, N., Simonds, E.F., White, L., Lacayo, N.J., Fantl, W.J., Fazio, G., et al. (2018). Single-cell developmental classification of B cell precursor acute lymphoblastic leukemia at diagnosis reveals predictors of relapse. Nat. Med. *24*, 474–483.
63. Sahaf, B., Pichavant, M., Lee, B.H., Duault, C., Thrash, E.M., Davila, M., Fernandez, N., Millerchip, K., Bentebibel, S.E., Haymaker, C., et al. (2021). Immune Profiling Mass Cytometry Assay Harmonization: Multicenter Experience from CIMAC-CIDC. Clin. Cancer Res. *27*, 5062–5071.
64. Finck, R., Simonds, E.F., Jager, A., Krishnaswamy, S., Sachs, K., Fantl, W., Pe'er, D., Nolan, G.P., and Bendall, S.C. (2013). Normalization of mass cytometry data with bead standards. Cytometry A. *83*, 483–494.
65. Lun, A.T.L., Richard, A.C., and Marioni, J.C. (2017). Testing for differential abundance in mass cytometry data. Nat. Methods *14*, 707–709.
66. Nowicka, M., Krieg, C., Crowell, H.L., Weber, L.M., Hartmann, F.J., Guglietta, S., Becher, B., Levesque, M.P., and Robinson, M.D. (2017). CyTOF workflow: differential discovery in high-throughput high-dimensional cytometry datasets. F1000Res. *6*, 748.
67. Van Gassen, S., Callebaut, B., Van Helden, M.J., Lambrecht, B.N., Demeester, P., Dhaene, T., and Saeys, Y. (2015). FlowSOM: Using self-organizing maps for visualization and interpretation of cytometry data. Cytometry A. *87*, 636–645.
68. Bates, D., Mächler, M., Bolker, B., and Walker, S. (2014). Fitting Linear Mixed-Effects Models using lme4. Preprint at arXiv. https://doi.org/10.48550/arXiv.1406.5823.
69. Angerer, P., Haghverdi, L., Büttner, M., Theis, F.J., Marr, C., and Buettner, F. (2016). destiny: diffusion maps for large-scale single-cell data in R. Bioinformatics *32*, 1241–1243.
70. Liaw, A., and Wiener, M.C. (2007). Classification and Regression by randomForest.
71. Kuhn, M. (2008). Building Predictive Models in R Using the caret Package. J. Stat. Software *28*, 1–26.
72. Dobin, A., Davis, C.A., Schlesinger, F., Drenkow, J., Zaleski, C., Jha, S., Batut, P., Chaisson, M., and Gingeras, T.R. (2013). STAR: ultrafast universal RNA-seq aligner. Bioinformatics *29*, 15–21.
73. Wang, L., Wang, S., and Li, W. (2012). RSeQC: quality control of RNA-seq experiments. Bioinformatics *28*, 2184–2185.
74. Patro, R., Duggal, G., Love, M.I., Irizarry, R.A., and Kingsford, C. (2017). Salmon provides fast and bias-aware quantification of transcript expression. Nat. Methods *14*, 417–419.

75. Love, M.I., Huber, W., and Anders, S. (2014). Moderated estimation of fold change and dispersion for RNA-seq data with DESeq2. Genome Biol. *15*, 550.

76. Yu, G., Wang, L.G., Han, Y., and He, Q.Y. (2012). clusterProfiler: an R package for comparing biological themes among gene clusters. OMICS *16*, 284–287.

77. Liberzon, A., Birger, C., Thorvaldsdóttir, H., Ghandi, M., Mesirov, J.P., and Tamayo, P. (2015). The Molecular Signatures Database (MSigDB) hallmark gene set collection. Cell Syst. *1*, 417–425.

78. Chen, B., Khodadoust, M.S., Liu, C.L., Newman, A.M., and Alizadeh, A.A. (2018). Profiling Tumor Infiltrating Immune Cells with CIBERSORT. Methods Mol. Biol. *1711*, 243–259.

79. Sturm, G., Finotello, F., and List, M. (2020). Immunedeconv: An R Package for Unified Access to Computational Methods for Estimating Immune Cell Fractions from Bulk RNA-Sequencing Data. Methods Mol. Biol. *2120*, 223–232.

80. Corces, M.R., Trevino, A.E., Hamilton, E.G., Greenside, P.G., Sinnott-Armstrong, N.A., Vesuna, S., Satpathy, A.T., Rubin, A.J., Montine, K.S., Wu, B., et al. (2017). An improved ATAC-seq protocol reduces background and enables interrogation of frozen tissues. Nat. Methods *14*, 959–962.

81. Smith, J.P., Corces, M.R., Xu, J., Reuter, V.P., Chang, H.Y., and Sheffield, N.C. (2021). PEPATAC: An optimized pipeline for ATAC-seq data analysis with serial alignments. Preprint at bioRxiv. https://doi.org/10.1101/2020.10.21.347054.

82. Ignatiadis, N., Klaus, B., Zaugg, J.B., and Huber, W. (2016). Data-driven hypothesis weighting increases detection power in genome-scale multiple testing. Nat. Methods *13*, 577–580.

83. Baskar, R., Chen, A.F., Favaro, P., Reynolds, W., Mueller, F., Borges, L., Jiang, S., Park, H.S., Kool, E.T., Greenleaf, W.J., and Bendall, S.C. (2022). Integrating transcription-factor abundance with chromatin accessibility in human erythroid lineage commitment. Cell Rep. Methods *2*, 100188.

STAR★METHODS

KEY RESOURCES TABLE

REAGENT or RESOURCE	SOURCE	IDENTIFIER
Antibodies		
Mouse anti-human CD45, clone HI30	BioLegend	Cat# 304002; RRID: AB_314390
Mouse anti-human HLA-DR, clone L243	BioLegend	Cat# 307602; RRID: AB_314680
Mouse anti-human CD41, clone HIP8	BioLegend	Cat# 303702; RRID: AB_314372
Mouse anti-human CD235a, clone HIR2	BioLegend	Cat# 306602; RRID: AB_314620
Mouse anti-human CD1c, clone L161	BioLegend	Cat# 331502; RRID: AB_1088996
Mouse anti-human CD19, clone HIB19	Standard BioTools	Cat # 3142001B; RRID: AB_2651155
Mouse anti-human CD123, clone 6H6	Standard BioTools	Cat # 314014B; RRID: AB_2811081
Mouse anti-human CD69, clone F50	Standard BioTools	Cat# 3144018B; RRID: AB_2687849
Mouse anti-human CD3, clone OKT3	BioLegend	Cat# 317302; RRID: AB_571927
Mouse anti-human CD11c, clone 3.9	Standard BioTools	Cat# 3146014B
Mouse anti-human CD182/CXCR2, clone 5E8	Standard BioTools	Cat# 3147010B
Mouse anti-human CD274/PDL1, clone 29E.2A3	Standard BioTools	Cat# 3148017B
Mouse anti-human CD45RA, clone HI100	BioLegend	Cat# 304143; RRID: AB_2562822
Mouse anti-human CD206, clone 15-2	BioLegend	Cat# 321102; RRID: AB_571923
Mouse anti-human CD103, clone Ber-ACT8	BioLegend	Cat# 3151011B; RRID: AB_2756418
Mouse anti-human CD66b, clone 80H3	Standard BioTools	Cat# 3152011B; RRID: AB_2661795
Mouse anti-human CD192/CCR2, clone K036C2	Standard BioTools	Cat# 3153023B
Mouse anti-human CD142, clone Ny2	BioLegend	Cat# 365202; RRID: AB_2564564
Mouse anti-human CD36, clone 5-271	Standard BioTools	Cat# 3155012B; RRID: AB_2756286
Mouse anti-human CXCR3, clone G025H7	Standard BioTools	Cat# 3156004B; RRID: AB_2687646
Mouse anti-human CD33, clone WM53	Standard BioTools	Cat# 3158001B; RRID: AB_2661799
Mouse anti-human CD357, clone 621	Standard BioTools	Cat# 3159020B; RRID: AB_2858232
Mouse anti-human CD14, clone M5E2	Standard BioTools	Cat# 3160001B; RRID: AB_2687634
Mouse Ultra-LEAF anti-human CD253 (Trail), clone RIK-2	BioLegend	Cat# 308213; RRID: AB_2814154
Mouse anti-human CD273 (PD-L2), clone MIH18	BioLegend	Cat# 345502; RRID: AB_1953319
Mouse anti-human CD33, clone WM53	Standard BioTools	Cat# 3163023B; RRID: AB_2687857
Mouse anti-human CD15/SSEA-1, clone W6D3	Standard BioTools	Cat# 3164001B; RRID: AB_2810970
Mouse anti-human CD16, clone 3G8	Standard BioTools	Cat# 3165001B; RRID: AB_2802109
Mouse anti-human CD279 (PD-1), clone EH12.2H7	BioLegend	Cat# 329902; RRID: AB_940488
Mouse anti-human CD197/CCR7, clone G043H7	Standard BioTools	Cat# 3167009A; RRID: AB_2858236
Mouse anti-human Lymphotoxin beta Receptor, clone 31G4D8	BioLegend	Cat# 322002; RRID: AB_2139071
Mouse anti-human Slan (M-DC8), clone DD-1	Miltenyi Biotec	Cat# 130-099-128; RRID: AB_2660075
Mouse anti-human CD152/CTLA4, clone 14D3	Standard BioTools	Cat# 3170005B; RRID: AB_2858238
Mouse anti-human CD9, clone SN4 C3-3A2	Standard BioTools	Cat# 3171009B; RRID: AB_2877094
Mouse anti-human Ki67, clone B56	Standard BioTools	Cat# 3172024B; RRID: AB_2858243
Mouse anti-human CD141 (Thrombomodulin), clone M80	BioLegend	Cat# 344102; RRID: AB_2201808
Mouse anti-human CD169 (Siglec-1), clone 7-239	BioLegend	Cat# 346002; RRID: AB_2189031
Mouse anti-human CD10, clone HI10a	BioLegend	Cat# 312202; RRID: AB_314913
Mouse anti-human CD56, clone NCAM16.2	Standard BioTools	Cat# 3176008B; RRID: AB_2938870
Mouse anti-human CD11b/Mac-1, clone ICRF44	Standard BioTools	Cat# 3209003B; RRID: AB_2687654
Mouse anti-human CD45, clone HI30	BioLegend	Cat# 304028; RRID: AB_893338
Mouse anti-human CD3, clone UCHT1	BioLegend	Cat# 300472; RRID: AB_2687178
Mouse anti-human CD4, clone SK3	BioLegend	Cat# 980812; RRID: AB_2820224

(*Continued on next page*)

Continued

REAGENT or RESOURCE	SOURCE	IDENTIFIER
Mouse anti-human CD8, clone SK1	BioLegend	Cat# 980902; RRID: AB_2616623
Mouse anti-human CD95, clone DX2	BioLegend	Cat# 305624; RRID: AB_2561830
Mouse anti-human CD45RA, clone HI100	StemCell	Cat# 100-0317
Mouse anti-human CD197 (CCR7), clone 150503	BD Biosciences	Cat# 561271; RRID: AB_1056167
Mouse anti-human CD62L (L-selectin), clone DREG-56	BD Biosciences	Cat# 562720; RRID: AB_2744441
Mouse anti-human CD25, clone M-A251	BioLegend	Cat# 356138; RRID: AB_2632781
Rat anti-mouse/human CD11b, clone M1/70	BioLegend	Cat# 101243; RRID: AB_2561373
Mouse anti-human CD33, clone P67.6	BioLegend	Cat# 366612; RRID: AB_2566405
Mouse anti-human CD14, clone 63D3	BioLegend	Cat# 367140; RRID: AB_2814323
Mouse anti-human CD15 (SSEA-1), clone W6D3	BioLegend	Cat# 323008; RRID: AB_756014
Mouse anti-human CD16, clone B73.1	BioLegend	Cat# 360710; RRID: AB_2562952
Mouse anti-human HLA-DR, clone L243	BioLegend	Cat# 307636; RRID: AB_2561831
Mouse anti-human CD183 (CXCR3), clone G025H7	BioLegend	Cat# 353706; RRID: AB_10962912
Mouse anti-human CD3, clone UCHT1	BioLegend	Cat# 300468; RRID: AB_2629574
Mouse anti-human Slan (M-DC8), clone DD-1	Miltenyi Biotec	Cat# 130-117-371; RRID: AB_2733608
Mouse anti-human Lineage Cocktail (CD3, CD20, CD19, CD56), clones UCHT1, HIB19, 2H7, 5.1H11	BioLegend	Cat# 363601; RRID: AB_2916117
Mouse anti-human CD66b, clone 6/40c	BioLegend	Cat# 392904; RRID: AB_2750201
Mouse anti-human CD45, clone HI30	Standard BioTools	Cat# 3089003B; RRID: AB_2938863
Mouse anti-human CD3, clone UCHT1	BioLegend	Cat# 300402; RRID: AB_314056
Mouse anti-human CD27, clone O323	BioLegend	Cat# 302839; RRID: AB_2562817
Mouse anti-human CD57, clone HCD57	BioLegend	Cat# 322325; RRID: AB_2563757
Mouse anti-human CD11b/Mac-1, clone ICRF44	Standard BioTools	Cat# 3144001B; RRID: AB_2714152
Mouse anti-human CD4, clone RPA-T4	Standard BioTools	Cat# 3145001B; RRID: AB_2661789
Mouse anti-human CD8, clone RPA-T8	Standard BioTools	Cat# 3146001B; RRID: AB_2687641
Mouse anti-human CD28, clone CD28.2	BioLegend	Cat# 302937; RRID: AB_2563737
Mouse anti-human CD274/PD-L1, clone 29E.2A3	Standard BioTools	Cat# 3175017B; RRID: AB_2687638
Mouse anti-human CD45RO, clone UCHL1	Standard BioTools	Cat# 3149001B; RRID: AB_2687851
Mouse anti-human CD134/OX40, clone ACT35	Standard BioTools	Cat# 3150023B; RRID: AB_2938869
Mouse anti-human CD244/2B4, clone C1.7	BioLegend	Cat# 329502; RRID: AB_1279194
Mouse anti-human CD38, clone HIT2	BioLegend	Cat# 303535; RRID: AB_2562819
Mouse anti-human TIGIT, clone MBSA43	Standard BioTools	Cat# 3153019B; RRID: AB_2756419
Mouse anti-human PARP, clone QA17A17	BioLegend	Cat# 669902; RRID: AB_2814517
Mouse anti-human CD183/CXCR3, clone G025H7	Standard BioTools	Cat# 3156004B; RRID: AB_2687646
Mouse anti-human CD137 (4-1BB), clone 4B4-1	Standard BioTools	Cat# 3158013B; RRID: AB_2888927
Mouse anti-human CD20, clone 2H7	BioLegend	Cat# 302302; RRID: AB_314250)
Mouse anti-human Tbet, clone 4B10	Standard BioTools	Cat# 3160010B; RRID: AB_2810251
Mouse anti-human CD152/CTLA-4, clone 14D3	Standard BioTools	Cat# 3161004B; RRID: AB_2687649
Mouse anti-human CD25, clone M-A251	Biolegend	Cat# 356102; RRID: AB_2561751
Mouse anti-human CD272/BTLA, clone MIH26	Standard BioTools	Cat# 3163009B; RRID: AB_2910546
Mouse anti-human CD39, clone A1	BioLegend	Cat# 328221; RRID: AB_2563747
Mouse anti-human CD223/LAG-3, clone 874501	Standard BioTools	Cat# 3165028B; RRID: AB_2687859
Mouse anti-human CD160, clone BY55	BioLegend	Cat# 341202; RRID: AB_2074411
Mouse anti-human CD197/CCR7, clone G043H7	Standard BioTools	Cat# 3167009A; RRID: AB_2858236
Mouse anti-human CD127/IL-7Ra, clone A019D5	Standard BioTools	Cat# 3168017B; RRID: AB_2756425
Mouse anti-human CD366/Tim-3, clone F38-2E2	Standard BioTools	Cat# 3169028B; RRID: AB_2905650
Mouse anti-human CD45RA, clone HI100	Standard BioTools	Cat# 3170010B; RRID: AB_2938862
Mouse anti-human Ki-67, clone Ki-67	BioLegend	Cat# 350502; RRID: AB_1066238

(*Continued on next page*)

Continued

REAGENT or RESOURCE	SOURCE	IDENTIFIER
Mouse anti-human C122/IL-2Rbeta, clone TU27	BioLegend	Cat# 339015; RRID: AB_2563712
Mouse anti-human CD95/Fas, clone DX29	BioLegend	Cat# 305631; RRID: AB_2563766
Hamster anti-human Helios, clone 22F6	BioLegend	Cat# 137202; RRID: AB_1090063
Mouse anti-human Eomes, clone WD1928	Thermo Fisher Scientific	Cat# 14-4877-82; RRID: AB_2572882
Mouse anti-human 279/PD-1, clone EH12.2H7	Standard BioTools	Cat# 3174020B; RRID: AB_2868402
Mouse anti-human CD16, clone 3G8	Standard BioTools	Cat# 3209002B; RRID: AB_2756431
Biological samples		
Patient apheresis, peripheral blood and GD2-CAR product samples from phase I trial	This paper	NCT02107963
Critical commercial assays		
Human Luminex XL Cytokine 45-Plex	RND Systems	LKTM014
Human IFN-gamma DuoSet ELISA	RND Systems	DY285B
Deposited data		
Bulk RNA-seq	This paper	dbGaP: phs003455.v1.p1
Bulk ATAC-seq	This paper	dbGaP: phs003455.v1.p1
Experimental models: Cell lines		
Human: THP-1 cells	ATCC	TIB-202
Human: 143B cells	ATCC	CRL-8303
Recombinant DNA		
iC9-2A-14G2A.CD28.OX40Z vector	Heczey et al.[11]	N/A
CXCR3-A Custom Vector	Twist Biosciences	NCBI Reference Sequence: NM_001504.2
Software and algorithms		
ChrAccR	Fabian Mueller, https://doi.org/10.5281/zenodo.6091218	https://github.com/GreenleafLab/ChrAccR, https://zenodo.org/record/6091218
DESeq2	Love et al.,[75] http://refhub.elsevier.com/S2667-2375(22)00043-1/sref35	https://bioconductor.org/packages/release/bioc/html/DESeq2.html
SAMtools	SAMtools	http://samtools.sourceforge.net/
Macs2	Zhang et al., 2008 http://refhub.elsevier.com/S1097-2765(21)00753-X/sref43	https://pypi.org/project/MACS2/
ChIPseeker	Yu et al., 2015 https://doi.org/10.1093/bioinformatics/btv145	https://bioconductor.org/packages/release/bioc/html/ChIPseeker.html
ChromVAR	Schep et al., 2017 https://www.nature.com/articles/nmeth.4401	https://bioconductor.org/packages/release/bioc/html/chromVAR.html
Seurat	Stuart et al., 2019 http://refhub.elsevier.com/S1097-2765(21)00753-X/sref38	https://github.com/satijalab/seurat/
CATALYST	Crowell et al., 2023 https://github.com/HelenaLC/CATALYST	https://www.bioconductor.org/packages/release/bioc/html/CATALYST.html
SingleCellExperiment	Amezquita et al., 2020 https://www.nature.com/articles/s41592-019-0654-x	https://bioconductor.org/packages/release/bioc/html/SingleCellExperiment.html
flowCORE	Ellis et al., 2023	https://bioconductor.org/packages/release/bioc/html/flowCore.html
caret	Kuhn et al., 2023 https://github.com/topepo/caret/	https://cran.r-project.org/web/packages/caret/index.html

(*Continued on next page*)

Continued

REAGENT or RESOURCE	SOURCE	IDENTIFIER
randomForest	Liaw et al., 2002 https://CRAN.R-project.org/doc/Rnews/	https://cran.r-project.org/web/packages/randomForest/index.html
Bead-based Normalizer	Finck et al.,[64]	https://med.virginia.edu/flow-cytometry-facility/wp-content/uploads/sites/170/2015/10/3_Finck-Rachel_CUGM_May2013.pdf
Single-Cell-Debarcoder	Fread et., 2017	https://github.com/zunderlab/single-cell-debarcoder
cydar	Lun et al.,[65]	https://www.bioconductor.org/packages/release/bioc/html/cydar.html
Lme4	Bates et al., 2015	https://cran.r-project.org/web/packages/lme4/index.html
Destiny	Angerer et al.,[69]	https://bioconductor.org/packages/release/bioc/html/destiny.html
RIMA	Liu et al., 2022	https://liulab-dfci.github.io/RIMA/
STAR	Dobin at al.,[72]	https://hbctraining.github.io/Intro-to-rnaseq-hpc-O2/lessons/03_alignment.html
RSeQC	Wang et al.,[73]	https://rseqc.sourceforge.net/
Salmon	Patro et al.,[74]	https://combine-lab.github.io/salmon/
ClusterProfile	Wu et al., 2021	https://github.com/YuLab-SMU/clusterProfiler
CIBERSORT	Chen et al.,[78]	https://cibersortx.stanford.edu/
Immunedeconv	Sturm et al.,[79]	https://github.com/omnideconv/immunedeconv

RESOURCE AVAILABILITY

Lead contact

Further information and requests for resources and reagents should be directed to and will be fulfilled by lead contact, Rosandra Kaplan(kaplanrn@mail.nih.gov).

Materials availability

This study did not generate new unique reagents.

Data and code availability

- RNA-seq and ATAC-seq data have been deposited in dbGAP and are available via controlled access as of the date of publication. Accession numbers are listed in the key resources table.
- This paper does not report any original code.
- Any additional information required to reanalyze the data reported in this paper is available from the lead contact upon request.

EXPERIMENTAL MODEL AND STUDY PARTICIPANT DETAILS

Trial design

This is a Phase I open labeled, single institution dose escalation trial of GD2 CAR-Ts in children and young adults with GD2+ solid tumors carried out in the Pediatric Oncology Branch of the National Cancer Institute (NCT02107963). The trial used a 3+3 design with four dose levels with administration of 1 x 10^5, 1 x 10^6, 3 x 10^6, and 1 x 10^7 transduced GD2 CAR-Ts/kg. The primary objectives were to determine the feasibility of producing GD2 CAR-Ts meeting the established release criteria and to assess the safety of administering escalating doses of GD2 CAR-Ts in children and young adults with neuroblastoma and osteosarcoma (eligibility criteria in Table S1), following cyclophosphamide-based lymphodepletion (Days -3 to -2: 1800 mg/m^2/day over 2 hours daily for 2 days), as well as determine the recommended Phase II dose and evaluate clinical kinetics of GD2 CAR-Ts. Secondary objectives included determining if administration of GD2 CAR-Ts mediated antitumor effects, and measuring correlates of CAR-T activity, including CAR expansion and persistence. The GD2 CAR construct also included an iC9, which could be activated by a bioinert small molecule dimerizing agent, AP1903, to mediate clearance of GD2 CAR-Ts. Secondary objectives included potential administering AP1903 for severe CAR-T toxicity and assessing toxicity of AP1903 if administered. Dose escalation decisions were made based on clinically significant dose-limiting toxicity (DLT) events possibly associated with CAR-T. DLTs were determined

during the first 28-days after CAR-T administration and defined as a treatment-emergent adverse event (TEAE) not reasonably attributed to the patient's underlying disease, other medical conditions, or concomitant medications or procedures. The maximum tolerated dose was defined as the highest dose level at which less than two of six evaluable patients experienced a DLT. Patients were eligible for enrollment if they had a confirmed diagnosis of osteosarcoma or neuroblastoma, two tumors which have ubiquitous expression of GD2.[19] All patients provided written informed consent before study entry. The study was approved by the relevant institutional review boards and/or independent ethics committees and was conducted according to the International Conference on Harmonization Good Clinical Practice guidelines and the Declaration of Helsinki. This study is registered with ClinicalTrials.gov.

METHOD DETAILS

CAR-T Cell manufacturing

Patients underwent apheresis to obtain autologous peripheral blood mononuclear cells (PBMCs). These cells were then selected using either bead selection or elutriation and ACK lysis, activated using CD3/CD28 beads, transduced with a bicistronic retroviral vector including an iC9 domain and a GD2.CD28.OX40.z CAR (Figure 1A), and then expanded for 7-9 days with IL-2.[23]

Cytokine assay

Cryopreserved plasma samples were analyzed for the presence of cytokines in a multiplex format according to the manufacturer's instructions (Human Luminex XL Cytokine 45-Plex R&D Systems.

qPCR assay

GD2 CAR-T expansion was measured by qPCR of peripheral blood-isolated PBMCs using TaqMan chemistry on the StepOnePlus™ Real-Time PCR System according to the manufacturer's instructions.

Target	Primer/Probe Name	Sequence (5'-3')
CDKN1A	Sense primer	GAAAGCTGACTGCCCCTATTTG
	Antisense primer	GAGAGGAAGTGCTGGGAACAAT
	Probe	CTCCCCAGTCTCTTT
OX40Z	Sense primer	CGCCCACTCCACCCT
	Antisense primer	GTTCTGGCCCTGCTGGTA
	Probe	CAAGATCAGAGTGAAGTTC

Mass cytometry, cytometry by time of flight (CyTOF), assay and analysis

Pre-treatment (apheresis), GD2 CAR-T product, and post-treatment (apheresis or whole blood) samples were analyzed by mass cytometry (CyTOF) with 2 different panels as previously described.[62,63]

CyTOF assays

Upon thawing, cells were washed twice with RPMI supplemented with penicillin-streptomycin and L-glutamine (Hyclone), 10% FBS (Hyclone), 20 U/mL of sodium heparin (Millipore Sigma) and benzonase 25 U/mL (Pierce, ThermoFisher). Cell counts were obtained using a Vi-Cell XR cell viability analyzer (Beckman Coulter), and cells were split to proceed with antibody staining with a range of 1 to 2 million cells per test. Reconstituted lyophilized Veri-Cells tagged with 181Ta (custom order from BioLegend) were added directly to each sample to a ratio of 1:10.

For the T cell Phenotype Panel, cells were washed twice in PBS (Rockland) and then were stained for live-dead discrimination with Cell-ID™ Cisplatin 5 mM (Fluidigm) for 5 min. After 2 washes with the Cell Staining Media (CSM, PBS 1X supplemented with 0.5% BSA and 0.02% sodium azide), cells were resuspended in 1X Maxpar® Fix I Buffer (Fluidigm) and fixed for 10 min at room temperature. Cells were washed twice with Maxpar 10X Barcode Perm Buffer (Fluidigm) and stained for barcoding with the Cell-ID™ 20-Plex Pd Barcoding Kit (Fluidigm) for 30 min at room temperature. Then, cells were washed twice with CSM prior to being pooled in a unique 5 mL FACS tube. The composite sample was stained with a surface antibody cocktail containing the Fc receptor-blocking solution Human TruStain FcX™ (BioLegend) for 30 min at room temperature. After 2 washes with CSM, cells were fixed in CSM + PFA 2% (Alfa-Aesar) for 10 min at room temperature and washed again in CSM. Then cells were fixed again with ice-cold methanol for 10 min on ice in the dark. After 2 washes with CSM, we proceeded to intracellular staining (Table S6) for 45 min at room temperature. Finally, after 2 washes in CSM, cells were stained with the Cell-ID Ir-Intercalator in 1X PBS (Rockland) + PFA 2% overnight at 4°C. Prior to acquisition on the next day, the sample was washed twice with CSM and 3 times with milli-Q water and resuspended with EQ Four Element Calibration Beads (Fluidigm) 1:10 in milli-Q water. Data were acquired on a Helios mass cytometer (Fluidigm). A mixture of unstimulated and PMA/ionomycin stimulated, tantalum-labeled lyophilized PBMCs (Vericells, Biolegend) were added to all samples as a spike-in control.

For Myeloid Panel, pre-treatment patient samples, post-treatment patient samples, and healthy human PBMC samples were thawed into RPMI media (Gibco) supplemented with 5% FBS (Omega Scientific). Samples were then washed twice with PBS (Corning) supplemented with 2% FBS. Cell counts were obtained using a Moxi V cell viability analyzer (Orflo). 10 million cells per sample were taken into viability staining with Cell-ID™ Cisplatin 5 μM (Fluidigm) in PBS. Cells were then washed with 1x CyPBS (Rockland) and blocked with Human Blocking Solution (1x CyPBS, 1mM EDTA, 1% Human AB Serum, 0.1% NaN3 in 1x CyPBS) for 10 min. Cells were then barcoded using triplet combinations of anti-human CD45 Cadmium metals (Fluidigm) in CyFACS (2mM EDTA, 0.1% BSA, 0.05% NaN3 in 1x CyPBS) for 30 minutes at 4°C. Cells were then washed twice with CyFACS and pooled into one tube. A total of 5 patient samples and 1 healthy PBMC technical control were barcoded and ran together for each CyTOF acquisition. Post-washes, cells were stained with an established Myeloid Panel in CyFACS for 30 min at 4°C. Cells were washed twice with CyFACS and resuspended in 2% PFA (Thermo Scientific) overnight at 4°C. Fixed cells were permeabilized with 1x Permeabilization Buffer (eBioscience) for 30 minutes at 4°C. Cells were then resuspended in Cell-ID™ Intercalator 500 μM (Fluidigm) in 1x Permeabilization Buffer for 30 min at room temperature. Cells were washed once with CyFACS and once with Cell Acquisition Buffer (Fluidigm), resuspended in 1:10 EQ Four Element Calibration Beads (Fluidigm) in Cell Acquisition Buffer, and CyTOF acquisitions were run.

RNA-sequencing assay and analysis

cDNA library construction

Total RNA was quantified using the Quant-iT™ RiboGreen® RNA Assay Kit and normalized to 5ng/ul. An aliquot of 200ng for each sample was transferred into library preparation which was an automated variant of the Illumina TruSeq™ Stranded mRNA Sample Preparation Kit. This method preserves the strand orientation of the RNA transcript and uses oligo dT beads to select mRNA from the total RNA sample. It is followed by heat fragmentation and cDNA synthesis from the RNA template. The resultant 500bp cDNA then goes through library preparation (end repair, base 'A' addition, adapter ligation, and enrichment) using Broad Institute-designed indexed adapters substituted in for multiplexing. After enrichment, the libraries were quantified with qPCR using the KAPA Library Quantification Kit for Illumina Sequencing Platforms and then pooled equimolarly. The entire process was performed in a 96-well format and all pipetting was done by either Agilent Bravo or Hamilton Starlet.

Illumina sequencing

Pooled libraries were normalized to 2nM and denatured using 0.1 N NaOH prior to sequencing. Flowcell cluster amplification and sequencing were performed according to the manufacturer's protocols using either the HiSeq 2000 or HiSeq 2500 machine. Each run was performed with 101bp paired-end reads, including an eight-base index barcode. Data were analyzed using the Broad Institute Picard Pipeline which includes de-multiplexing and data aggregation.

ATAC-seq assay and analysis

ATAC-seq assay

Assay for Transposase-Accessible Chromatin with high-throughput sequencing (ATAC-seq) was conducted as previously described[80] with minor modifications specified below. Apheresis and Product samples were counted, and 150,000 cells were split into 3 replicates containing 50,000 cells each. Cells were pre-treated with 200 units/ml Dnase I (Worthington Biochemical, LS006343) in PBS for 30 min at 37°C. Post-incubation, samples were washed twice with ATAC resuspension buffer (ATAC-RSB; containing 1M Tris-HCl pH 7.5, 5M NaCl, 1M $MgCl_2$ in sterile water), plus 0.1% Tween-20, with centrifugation at 500g for 5 minutes at 4°C. Cells were then lysed for 3 minutes on ice with 50 μl cold ATAC-RSB plus 0.1% NP40, 0.1% Tween-20 and 0.01% Digitonin. After lysis, nuclei were washed with 1 ml ATAC-RSB containing 0.1% Tween-20 and were pelleted at 500g for 10 minutes at 4°C. Nuclei were transposed with Illumina Tn5 transposase (Illumina, 20034198), and reactions were cleaned up with the Qiagen MinElute PCR Purification Kit (Qiagen 28006). ATAC libraries were PCR amplified with New England Biosystems' 1X PCR Master Mix (NEB, M0541L) and custom Nextera PCR primers at 1.25 μM each for 11 or 12 total cycles. Amplified libraries were purified with AMPure XP beads (Beckman Coulter A63880), and the KAPA library quantification kit (Kapa Biosystems, KK4854) was used to quantify library concentrations. Libraries were pooled with equimolar concentrations and sequenced by Novogene on a Novaseq S4 with 2x150bp paired-end reads.

Primary monocyte assays

Healthy donor monocytes were isolated from healthy donor apheresis by counterflow elutriation and acquired from the NIH Clinical Center Department of Transfusion Medicine and cryopreserved. Monocytes were thawed and treated with varying concentrations of recombinant human IFN α or IFN γ and cultured at 37°C/5%CO_2 for 24 hours. CXCR3 expression was analyzed by flow cytometry gated on single, live, $CD45^+$ $CD33^+$ cells.

Cell lines

THP-1 monocyte cells were acquired from ATCC and cultured in ATCC-formulated RPMI-1640 medium with 10% FBS, 100 units/mL penicillin-streptomycin, and 0.05 mM 2-mercaptoethanol. A CXCR3-overexpressing THP-1 cell line (CXCR3 THP-1) was generated by lentiviral transduction. Briefly, a plasmid containing human CXCR3-A (GenBank: NM_001504.2) was synthesized (Twist Biosciences) and lentivirus was produced as previously described.[21] THP1 cells were centrifuged in the presence of lentivirus and 8 mg/mL polybrene at 931 xg for 2 hours at 30C. Lentivirus was washed off the following day and CXCR3 expression was confirmed by flow cytometry (Figure S6E). 143B osteosarcoma tumor cells were acquired from ATCC and cultured in RPMI-1640 medium with 10% FBS, 100 units/mL penicillin-streptomycin. GD2-CAR T cells from healthy donors were manufactured as previously described[22]

by the Biopharmaceutical Development Program, Frederick National Laboratory. GD2-CAR T cells were thawed and cultured overnight in T cell expansion media (TCEM; AIM-V media supplemented with 5% FBS, 2mM GlutaMAX, 14 mM HEPES) with 100 units/mL human recombinant IL-2.

Co-culture assays

Parental untransduced THP-1 (UTD THP-1), CXCR3 THP-1, 143B, and GD2CAR- T cells were harvested and resuspended in TCEM. Cell were cultured at indicated ratios for approximately 24 hours, at which point supernatant was collected and the cells were stained for flow cytometry. Human interferon gamma was analyzed by ELISA (R&D Systems).

Disease burden assessments

Disease burden score

There is no standard assessment method to describe the overall tumor burden of patients with relapsed or refractory disease. The tumor burden of patients enrolled on this trial ranged widely between newly relapsed patients with relatively small tumors and those with advanced, multiply relapsed, and refractory disease. With the goal of better characterizing this heterogeneous group of patients, we developed a preliminary radiographical disease burden score that considers the size of the largest tumor lesion, the number of metastatic lesions greater than or equal to one centimeter in size, and the number of sites involved. Our scoring system is included in Table 2. For the sake of comparison, patients who were assigned a total score less than or equal to 2 were classified as having small disease burden. In contrast, patients with a score of 3 or above were classified as having large disease burden.

Assay for quantification of metabolically active tumor burden

Standardized Uptake Values (SUVs) were calculated as the ratio of measured activity to injected dose per body weight (kilogram). All lesions identified by nuclear medicine physicians during standard read-out and reviewed per protocol analysis were considered for quantitative analysis. Semi-automated analysis was performed using commercial software (MIM, Cleveland, OH, USA). Briefly, a region-growing technique available within MIM software was utilized starting from seed point using bookmarks provided from clinical imaging reports. Briefly, region-growing iteratively adds image voxels to the contour if they meet a uniformity criterion and values derived from existing voxels contained within the contour.[28] This algorithm was optimized based on anatomical region by varying the minimum uptake bound for which contour stops searching (range 1-2 SUV). In any cases of algorithm failure, threshold-based segmentation from minimum 2 SUV is accepted. For all lesions, SUV metrics were extracted, including: SUV_{max}, SUV_{mean}, Total Lesion Glycolysis (TLG), and lesion volume. Additionally, metrics from all lesions were aggregated for patient-level analysis, including: SUV_{max}, defined as maximum uptake value of all lesion SUV_{max} values, TLG, defined as sum of all lesion TLG values, and volume, defined as the sum of all lesion volumes.

QUANTIFICATION AND STATISTICAL ANALYSIS

CyTOF analysis

For the T cell Phenotype Panel, after CyTOF acquisition, the data collected were normalized using the Nolan Lab normalizer (https://github.com/nolanlab/bead-normalization/releases). Samples from the T cell Phenotype Panel were deconvoluted with the Zunder Lab Single Cell Debarcoder (https://github.com/zunderlab/single-cell-debarcoder).

For the Myeloid Panel, during data acquisition, a CD45-barcoding method was used to add healthy PBMCs as a technical control to the samples. After bead-based normalization using the Normalizer,[64] only live and singlet cells were included in the analysis. Data were batch corrected with a quantile function constructed for the pooled distribution of each batch (a pair of sample and spike-in control) using the cydar package.[65]

Analyses of the T cell Phenotype Panel data and the Myeloid Panel data followed the same pipeline. Data were arcsinh transformed (cofactor=5) and The CATALYST package[66] was used to apply the FlowSOM method[67] to cluster the cells and project the cells on the UMAP. Cell types were identified using lineage markers (Tables S6 and S7). Most clusters were present in each patient. The Generalized Linear Mixed Model (GLMM), through the lme4 package,[68] was used to identify significant differential cell population abundances. Correlations between cell type frequencies and peak GD2 CAR-T expansion (GD2 CAR copy numbers per 100ng of detected DNA) and tumor volume were performed using Spearman rank correlation tests. For the myeloid analysis, diffusion map pseudo-time was performed for trajectory analysis using the destiny package.[69] We conducted two separate trajectory analyses to differentiate between good and poor CAR-T expanders.

In the analyses of both CyTOF panel datasets, a machine learning (ML) strategy was implemented to discover the genes that can effectively discriminate between different conditions. To accomplish this goal, the importance scores of the genes were determined by training a random forest (RF) model using the normalized gene expression from the same number of randomly selected cells from each condition using the Caret and Random Forest R packages.[70,71] This procedure was repeated for 30 iterations and the importance scores of the genes in each iteration were scaled to the 0-100 range for a better comparison. When classifying the groups, a higher score is regarded as having more classification power.

RNA-seq analysis

Paired-end transcriptome reads were processed with a standardized RNA-seq Immune Analysis pipeline called RIMA (https://liulab-dfci.github.io/RIMA). RIMA is an automated Snakemake pipeline to streamline the processing of RNA-seq data. Read alignments

were performed with STAR[72] against the hg38 reference genome from the NCI Genomic Data Commons (GDC). RNA-seq quality control was performed on the aligned BAM files using RSeQC.[73] With the uniquely mapped reads, transcriptome per million (TPM) metrics were quantified using SALMON[74] on the BAM files. Differentially expressed genes were identified using DESeq2.[75] Gene set enrichment was performed using ClusterProfile[76] against Hallmark and ImmuneSigDB gene sets from the Molecular Signature Database (MsigDB).[77] Immune infiltration analysis was performed using CIBERSORT absolute[78] from the Immunedeconv[79] R package. Gene expression was first normalized by subtracting the average expression across samples, and the gene signature score was then calculated as the average normalized expression of gene sets. Wilcoxon rank-sum test was then applied to the gene signature scores.

The Exhaustion Score was derived by analyzing data from a previously described CAR-T model of exhaustion.[29] Differential analysis was performed on RNA-seq data from HA and CD19 CAR T cells cultured at the latest timepoint, when activation markers normalize (Day 14). Overlapping genes were selected that were differentially expressed (False Discovery Rate (FDR) p-value < 0.05). These genes defined the Exhaustion Score, comprising 553 genes. The Exhaustion Score was derived as a z-score of the geometric mean of expression values from this gene signature. The Activation Score was derived as a z-score of the geometric mean of expression values from the gene signature of T cell activation from the Panther Pathways dataset (Gene Ontology: GO_0042110).

Expression analysis on publicly available datasets

The results published here are in part based upon data generated by the Therapeutically Applicable Research to Generate Effective Treatments (TARGET) initiative, phs000218, managed by the NCI. The data used for this analysis are available at dbGaP accession phs000468.v21.p8. Information about TARGET can be found at http://ocg.cancer.gov/programs/target. Survival data and mRNA expression levels for CXCR3 and its ligands were downloaded from the TARGET Osteosarcoma cohort on the UCSC Xena browser.[52] High, middle, and low CXCR3 level groups were divided into similar-sized groups, and the proportional hazards ratio assumption required for Kaplan-Meier analyses was met and representative of the correct p-value assessment. Kaplan-Meier curves for high, medium, and low transcript levels were generated for analysis of overall survival of 85 patients for whom data were available. Statistical analysis on group survival differences was performed utilizing the log-rank test, and log-log plot confirmed that proportional hazards assumption was met (Figure S6C). Further, Cox proportional hazards model analysis demonstrated that low-level CXCR3 has an HR coefficient of 1.4755 compared to high-level CXCR3 (p=0.011) (Figure S6D).

ATAC-seq analysis

Raw fastq data from Novogene were processed with the pepATAC pipeline with standard parameters.[81] Quality control (QC) metrics such as Transcription Start Site (TSS) scores were calculated based on transcription start sites of protein-coding genes as indicated in hg38 gencode. Peaks were called using MACS2 with the following parameters on Tn5 insertion sites: –shift, -75, –extsize, 150, –nomodel, –call-summits, –nolambda'', -p, 0.01. Downstream analysis with the ChrAccR R package was carried out on the deduplicated bam files and MACS2 peak-called bed files output from pepATAC. The consensus peakset across technical and biological replicates was calculated using the getPeakSet.snakeATAC function in the ChrAccR R package where peaks had to be consistently absent or present with a cutoff of 0.75 (75%) across replicates to be retained. The count matrix was calculated as insertion counts across samples at consensus peakset regions using the ChrAccR region Aggregation function (Figure S4). DESeq2[75] was used to calculate differentially accessible peaks and independent hypothesis weighting[82] was used to correct for multiple testing. The ggmaplot package was used to visualize the MA plot. Differentially accessible peaks for samples classified as good or poor expanders were used to calculate motif enrichment using the getMotifEnrichment function in the ChrAccR R package based on the CIS-BP TF motif database (from chromVARmotifs package).[83] Adjusted p values (q values) were converted to -log(q value) and top enriched motifs were plotted by -log(q value) and odds ratio.

ADDITIONAL RESOURCES

Clinical trial information: https://clinicaltrials.gov/study/NCT02107963.